TET1 potentiates human iPS cell reprogramming

by rectifying extraembryonic gene noises

Makoto Motono[1,2,4,*], Keiko Hiraki-Kamon[1,4], Masayoshi Kamon[1], Hidenori Kiyosawa[3], Yoichi Kondo[2], and Hidemasa Kato[1,5,*]

[1]Department of Developmental Biology and Functional Genomics, Ehime University Graduate School of Medicine, Toon, Ehime, 791-0295, Japan.

[2]Department of Anatomy and Cell Biology, Osaka Medical and Pharmaceutical University, 2-7, Daigakumachi, Takatsuki, Osaka, 569-8686, Japan.

[3]Department of Life Science, Chiba Institute of Technology, 2-17-1, Tsudanuma, Narashino, Chiba, 275-0016, Japan.

[4]These authors contributed equally

[5]Lead Contact

[*]Correspondence: makoto.motono@ompu.ac.jp (M.M.), hidemasa.kato.zz@ehime-u.ac.jp (H. Kato)

SUMMARY

Induced pluripotent stem cells (iPSCs) exhibit inconsistent differentiation potential, negatively impacting their downstream applications. Here, we potentiated their reprogramming by adding ten-eleven translocation 1 (TET1), a DNA demethylase, to produce TET1-iPSCs (T-iPSCs). By comparing the differentiation efficiencies of 46 in-house-generated iPSC clones, we identified an extraembryonic gene signature linked to differentiation defects. The extraembryonic signature was upregulated when all three *TET* genes were knocked out in human embryonic stem cells. T-iPSCs with enhanced

epithelialized morphology, a trait attributable to TET1 activity during reprogramming, exhibited uniform *TET1* expression and lacked the identified extraembryonic signature. These T-iPSCs differentiated into ventral midbrain dopaminergic neurons with unprecedented fidelity and efficiency. Our data collectively revealed a deviation from the genuine embryonic gene profile in conventional human iPSCs, which was amendable by including TET1 in the reprogramming cocktail. We recommend the proposed T-iPSC production pipeline as a *de facto* standard for human iPSC reprogramming.

KEYWORDS

TET1, reprogramming, epithelial colony, default differentiation, extraembryonic lineage, ventral midbrain, dopaminergic neurons, BMP, WNT

INTRODUCTION

Human pluripotent stem cells (hPSCs) exhibit heterogeneous differentiation capabilities, a tendency usually more pronounced in human induced pluripotent stem cells (hiPSCs) (Koyanagi-Aoi et al., 2013; Ohnuki et al., 2014) than in human embryonic stem cells (hESCs) (Osafune et al., 2008). Previous data have shown that the expression levels of miR-371/2/3, stage-specific embryonic antigen (SSEA) 3/4, and TRA1-60 in hPSCs are correlated negatively with their differentiation capabilities, although SSEA3/4 and TRA1-60 are considered pluripotent markers for hPSCs (Kim et al., 2011). Superfluous LTR7-retrovirus-driven transcription has been reported as a risk factor for defective differentiation (Koyanagi-Aoi et al., 2013; Ohnuki et al., 2014). Furthermore, hiPSCs have hotspots of aberrant epigenomic reprogramming that are maintained after differentiation (Lister et al., 2011). The expression of *KLF4* appeared to be partly responsible for differentiation defects or epigenetic abnormalities (Kim et al., 2011; Lister et al., 2011; Ohnuki et al., 2014).

The mesenchymal-epithelial transition (MET) is crucial during the early phase of iPSC reprogramming from fibroblasts (Li et al., 2010), and ten-eleven translocation (TET) dioxygenases, the DNA demethylases, are crucial to MET (Hu et al., 2014). Although Tet1 expression begins in the early stages of mouse reprogramming where E-cadherin-positive epithelialized cells appear within the first week (Bartoccetti et al., 2020; Li et al., 2010; Samavarchi-Tehrani et al., 2010), human TET1 expression occurs later and to a moderate extent, which may lead to retarded epithelialization (Cacchiarelli et al., 2015). Moreover, early Tet1 induction during iPSC reprogramming is essential for unleashing the differentiation potential of mouse iPSCs by demethylating enhancers (Bartoccetti et al., 2020). Therefore, it is arguable that Yamanaka factors alone may be insufficient to demethylate the human genome of mesenchymal cells to attain bonafide pluripotency.

Parkinson's disease has drawn considerable research attention on ventral midbrain dopaminergic (mDA) neurons, including methods for inducing these cells *in vitro* from iPSCs (Barker et al., 2017; Steinbeck et al., 2015). Many laboratories employ dual SMAD inhibition (Chambers et al., 2009), which improves the neural differentiation efficiency of a wide variety of hiPSC clones, posited to be more refractory to neural induction than hESCs (Tchieu et al., 2017). However, it is unclear if dual SMAD inhibition may also impact later differentiation events, such as the regional patterning of the neural progenitors and neuronal maturation. Moreover, a previous study indicated that the *in vitro*-derived mDA cells differed substantially from their *in vivo* counterparts in their global expression profiles (La Manno et al., 2016), so further improvement of the pipeline for obtaining ventral mDA neurons is needed.

Here, we aimed to underpin the cause of the differentiation defects of current hiPSCs by studying the transcriptional profiles of these cells. By individually default-differentiating the hiPSC clone, we found statistical significance in the expression of *KLF4* to correlate to differentiation defects. We also found that KLF4-target genes were expressed in the extraembryonic tissues but little in the late epiblast. Importantly, this derepression of extraembryonic genes could be rectified if TET1 was uniformly expressed, a unique trait of our TET1-aided iPSCs (T-iPSCs), which differentiated into ventral mDA neurons with unprecedented fidelity and efficiency. Following the newly developed T-iPSC production pipeline, we hope that hiPSC might regain its prime position as the regenerative medicine and drug discovery cell source.

RESULTS

TET1-aided Human Cell Reprogramming

Given the benefits of TET1 in reprogramming and pluripotency (Bartoccetti et al., 2020; Verma et al., 2018), we generated episomal hiPSCs from male neonatal and female embryonic fibroblasts using the conventional reprogramming vectors (Okita et al., 2011) with or without *TET1*-overexpression (Figure 1A). We denote TET1-aided iPSCs as T-iPSCs and conventional iPSCs as C-iPSCs. We adopted reprogramming culture conditions established by Thomson's group (Chen et al., 2011), which enabled the passage of cells after trypsin digestion and trituration onto a non-feeder surface for better discrimination of the morphological aspects of clones (Figure 1B; see STAR Methods). T-iPSCs and C-iPSCs were induced in parallel by the same experimenter(s), using an equal number of starting fibroblasts for each induction. Colonies were selected for further expansion after approximately 28 days. Most of the emerging T-iPSC colonies exhibited an epithelialized morphology, but these epithelialized colonies were rare in the C-iPSCs (Figures 1C and 1D). Retrospective analyses

revealed that only some of the selected epithelialized colonies had good differentiation capabilities; therefore, we discarded the mesenchymal-like colonies with fuzzy borders (Figure 1C). Upon expansion in culture, we eliminated revertant clones with mesenchymal-like morphologies (Figure S1) as a dimorphic morphology reappeared, even if the seemingly epithelialized part of the colony had been lifted and subcultured. Coincidentally, a significant proportion of clones lost their vigorous cell-proliferation capacities. Therefore, we considered clones that reached more than 90% confluency in a 100-mm dish to be "established." In this manner, we established 121 T-iPSC clones (of 454 colonies) and 13 C-iPSC clones (of 72 colonies), which indicated a clear over-representation of T-iPSC clones.

Residual reprogramming vectors can negatively influence cell differentiation (Koyanagi-Aoi et al., 2013) or potentiate carcinogenesis upon transplantation (Ohnishi et al., 2014). We detected residual episomal plasmids using conventional polymerase chain reaction (PCR) (data not shown) (Yu et al., 2009). When we switched to quantitative PCR (qPCR), we found that conventional PCR only detected clones with >0.16 plasmid copies/genome as positive. The mean copy number of "vector-free" clones (as determined by conventional PCR) was 0.0062 ± 0.0067 (mean ± standard deviation; Figure 1E). Among these clones, we correlated the residual vector copy number with neural markers after default differentiation on day 8 (Figures 2B and 2C) and found no significant trend (data not shown). We deduced that a residual episomal copy number of <0.03, the maximal value among vector-free clones, should not affect the differentiation capability and tentatively used 0.03 as the vector-free status threshold.

We obtained 22 male isogenic vector-free clones (3 C-iPSCs and 19 T-iPSCs out of 526 colonies) and 24 female clones (3 C-iPSCs and 21 T-iPSCs out of 566 colonies) from five independent parallel inductions.

Transcriptomic Features Affecting Differentiation Efficiency

It is common to investigate the expression of "pluripotency-associated" genes in established iPSC clones (International Stem Cell et al., 2007). We analyzed the expression of *POU5F1*, *SOX2*, *NANOG*, *KLF4*, *MYC,* and *MYCN* in all clones in the undifferentiated state (day 0) (Figure 2B). No variance over 2-fold from the average was observed for *POU5F1, SOX2, NANOG,* or *MYC* (except for the 2T1 clone; Figures S2A and S2B). This analysis was performed in low-passage iPSC lines (passages 5 to 6), which are known to be prone to transcriptional noise (Chin et al., 2009). The averaged expression of the pluripotency-associated factors demonstrated the overall uniformity of the obtained hiPSC clones, which conformed to the qualitative criteria of pluripotency (Fogarty et al., 2017) (Figures 3A, S2A, and S2B). By contrast, the expression of *MYCN* and *KLF4* exhibited considerable fluctuations (Figure 2A).

Assessing Inherent Differentiation Capabilities using Default Neural Induction

We independently investigated the differentiation capabilities of integration-free hiPSCs (Figure 2B). We chose the default model of neural induction as the test method, representing an evolutionarily conserved developmental trajectory among vertebrates. This model advocated that dissociated early embryonic cells defaulted to neural induction when incubated in a developmentally neutral culture medium (Ozair et al., 2013). Along with other researchers, we have previously shown that mouse, monkey, and human ESCs robustly

default to neurogenesis under the conditions used herein (Bouhon et al., 2005; Ono et al., 2014; Patani et al., 2009).

This survey revealed striking differences in the differentiation capabilities of isogenic cell lines. We retrospectively set the 1T47 clone as our standard T-iPSC clone because it has the highest differentiation potential to ventral mDA neurons of all the clones we have tested and named it "differentiation-elite." The neural progenitor master regulator *PAX6* (Zhang et al., 2010) and radial glial cell marker *HES5* (Tchieu et al., 2017) were expressed at levels comparable to those in the 1T47 clone in only one-fourth of the clones (Figure 2C). Uniform-sized dense spheres or spheres with sac-like structures showed high or low differentiation capabilities to the neural lineage, respectively (Figure S3).

NANOG is a direct inhibitor of neural induction (Loh and Lim, 2011), and TBXT is expressed in the mesendoderm and non-neuronal ectoderm (Sasaki et al., 2016) in humans; therefore, we examined the expression of these markers after differentiation. Some cell lines exhibited relatively high expression levels of *NANOG* or *TBXT* after differentiation, which provided additional evidence of deviation from default neurogenesis (Figure 2D).

Our results show that approximately three-fourths of the established hiPSC clones still had inherent differentiation defects even if we chose vector-free epithelialized colonies. Given that our hiPSC clones were derived from isogenic fibroblasts, inter-clonal variations in their differentiation capabilities were barely attributable to genotype variations (Liang and Zhang, 2013). We excluded cell lines exhibiting high *NANOG* or *TBXT* expression after differentiation and named the hiPSC clones with satisfactory default differentiation

propensities as “default-elite” clones (Figures 2C and 2D). The default-elite clones and their karyotypes are shown in Figure S4.

Next, we investigated the correlations between gene expression levels before and after default differentiation (Figure 3A). As expected, the classical pluripotency-associated genes (*POU5F1*, *SOX2*, and *NANOG*) showed no significant correlations with the neural differentiation markers (Figure 3A). Contrastingly, the fluctuating expression of endogenous *KLF4* and *MYCN* in the undifferentiated state (Figure 2A) correlated negatively with the neural markers upon differentiation (Figures 3A and 3B). The observed negative correlation of *KLF4* expression to differentiation outputs provides the first quantitative and statistical evidence consolidating previous findings (Kim et al., 2011; Lister et al., 2013; Ohnuki et al., 2014).

We, therefore, analyzed candidate KLF4-activated genes during reprogramming. Based on a previously reported secondary hiPSC derivation system (Cacchiarelli et al., 2015), we posited *NLRP7*, *DPPA3*, and *DNMT3L* genes as candidate KLF4 targets. The expression of *NLRP7* and *DNMT3L* before differentiation showed a negative correlation with the neural markers after differentiation (Figures 3A and 3B). *HHLA1*, *ARRB1*, *FZD10*, and *GBX2* (Ohnuki et al., 2014), which have previously been associated with differentiation defects, did not correlate with the neural markers (Figure 3A). This discrepancy may be due to the different passage numbers of iPSCs when the markers were evaluated. We also examined *HAND1* as a candidate marker for partial reprogramming (Cacchiarelli et al., 2015). *HAND1* was strongly negatively correlated with the neural markers (Figures 3A and 3B).

Derepression of Extraembryonic Genes in Differentiation-Resistant Clones

We analyzed the expression patterns of several differentiation-resistant markers (including *HAND1*, *KLF4*, *MYCN*, *NLRP7*, and *DNMT3L*) within the human developmental context using published single-cell RNA-sequencing (scRNA-seq) data obtained from cultured human blastocysts (Xiang et al., 2020) or gastrulating embryo (Tyser et al., 2021). Surprisingly, most of the differentiation-resistant markers (*MYCN*, *KLF4*, *NLRP7*, and *HAND1*) were expressed in the extraembryonic compartments (amniotic epithelium [AME] or intermediate state cells [intermediate]) but only at low levels in the late epiblasts of the cultured embryos (Figures 4A and 4B). The mixed embryonic and extraembryonic transcriptome of the hiPSC clones suggests an intriguing possibility that human pluripotency may exist in a bistable state between the late epiblasts and extraembryonic lineages.

To directly assess this, we analyzed the single-cell transcriptome of our representative default-elite hiPSCs. The integrated data obtained from three default-elite hiPSC clones (1T47, 6T9, and 6C6), when displayed using uniform manifold approximation and projection (UMAP) dimension reduction (Figure 4C), were grouped into nine clusters (Figure 4D). The 6T9 and 6C6 clones co-clustered (main clusters 1 and 6) versus 1T47 (spread over the remaining clusters), revealing the proposed bistability (Figure 4D). Surprisingly, cluster 1, which was mainly represented by the 6T9 and 6C6 cells, exhibited an exclusive expression of representative amnion markers (including *BMP4*, *ACTC1*, and *GATA3*) (Figures 4B and 4E) (Chhabra and Warmflash, 2021; Xiang et al., 2020). The observed *BMP4* expression may have profound effects on the pluripotent state of the hiPSCs as it is an autocrine inducer of the amnion (Sasaki et al., 2016; Zheng et al., 2019). Furthermore, an epithelial-mesenchymal transition-related marker—*TWIST1*, expressed in the human extraembryonic compartment (Figure 4B)—was also overly expressed in cluster 1 (Figure 4E). The pro-mesenchymal trait is reminiscent of the mesenchymal revertants observed during the reprogramming process

(Figure S1) and the "flatter" appearance of 6T9/6C6 clones in culture (data not shown). Conversely, the expression levels of *SOX2*, *TET1,* and, to some extent, *NANOG* were low in these cells, which is consistent with the downregulation of SOX2 in the nascent amnions of monkeys (Sasaki et al., 2016). Notably, the expression level of *POU5F1* was relatively uniform among the clusters, suggesting that all cells retained a certain degree of pluripotency (Figure 4E).

Given the lower expression of *TET1* in a subpopulation of 6T9 and 6C6 cells, we analyzed RNA-seq data for TET1, TET2, and TET3-triple-knockout (TET-TKO) hESCs where all the TETs were knocked out in HUES8 hESCs (Charlton et al., 2020). Strikingly, TET-TKO hESCs exhibited augmented expression of the extraembryonic markers (*BMP4*, *GATA3*, and *TWIST1*) and *KLF4* (Figures 4F and 4G). Moreover, previously assigned differentiation-defective markers, such as *HHLA1*, *ABHD12B*, and *LINC-ROR,* were over-expressed in TET-TKO (Figures 4F and 4G) (Koyanagi-Aoi et al., 2013). Serendipitously, an over-representation of WNT agonists (WNT5A and WNT5B) in TET-TKO cells was observed in addition to BMP4, somewhat reminiscent of the inherent WNT hyper-activities in human PSCs (Blauwkamp et al., 2012). Our clone-by-clone inspection of the expression of these markers strongly supported that lower expression of *TET1* in the subpopulations of cells might be responsible for the aberrant expression of the marker genes (Figures 4G and S5).

An exciting finding concerning the extraembryonic marker's expressivity is their expression dynamics upon cell passaging. Aberrant *KLF4* expression, just after iPSC establishment (Figure 2A), was soothed down at later passages (Figure 4G), but the expression ratio was maintained among the clones. By contrast, the differential expression of *BMP4* and *HHLA1* among clones became evident only in later passages (compare Figures 4G, S5B, and S5C).

Global inspection of such markers showed that only the expression profile of KLF4 was maintained through passages. This trend suggests that such expressivity was settled during the reprogramming process.

We conjectured whether the observed extraembryonic gene expression levels were productive for differentiation toward such lineages. To this end, we differentiated the amniotic lineage according to the methods described earlier (Zheng et al., 2019). The expression levels of the extraembryonic genes in the induced cells were much higher than those in the undifferentiated state (Figure S5D). These results strongly suggested that the aberrant extraembryonic profiles of the hiPSC clones resulted from a derepression of such genes, deviating from the proper late epiblast's transcriptome.

Our data demonstrated that an extraembryonic-like differentiation signature within the *SOX2*/*TET1*-low subpopulation could be observed among hiPSC clones (Figures 4E and 4F).

Exerting Complete Differentiation of Ventral mDA Neurons

Next, we explored the differentiation potential of the clones beyond the early neural stages exerted by default differentiation (Figure 2C). To this end, we chose the ventral mDA neuron specification.

During development, the regionalization of the central nervous system occurs through the successive specification of the anteroposterior (AP) and dorsoventral (DV) axes (Tao and Zhang, 2016). Mouse midbrain AP coordinates are set by isthmus-derived FGF8-signaling and autocrine WNT-signaling cues (Arenas et al., 2015). The ventralization of midbrain precursors is mediated by Sonic Hedgehog (SHH) signaling, which emanates initially from

the notochord. In this study, we employed a rationale-based protocol developed in Studer's lab (Steinbeck et al., 2015) with minor modifications to derive ventral mDA neurons (Figure S6A; see STAR Methods).

We began by investigating the differences in the differentiation capabilities between our standard differentiation-elite clone (1T47) and randomly selected non-elite clones (2C10, 4T17, 6C7, and 6T8). We carefully avoided counting dead cells by studying pyknotic nuclei combined with beta-tubulin 3 (TuJ1) immunostaining (Figure S7). On day 19 of the differentiation process, we analyzed the expression of FOXA2, a floor plate-associated transcription factor and known precursor marker for mDA neurons (Ferri et al., 2007). Non-default-elite clones differentiated less efficiently toward FOXA2-positive cells than the 1T47 cells (Figure S6B). FOXA2-ventral progenitors acquire LMX1A in the ventral midbrain (Arenas et al., 2015). The proportion of the LMX1A-inducibility of 1T47 cells (88.5% ± 1.47%, Figure S6C) was as good as the best results reported previously using standard hESCs (H9) (Steinbeck et al., 2015).

To explore the identities of the LMX1A-negative cells, we analyzed NKX6-1 and PAX6, which are expressed in the adjacent dorsal regions of the mouse midbrain (Andersson et al., 2006). The proportions of the NKX6-1- and PAX6-positive cells were 8.78% ± 2.98% and 3.80% ± 1.19%, respectively (Figures S6C and S6D). NKX6-1/PAX6 double-positive cells were rare (<0.07%) (Figure S6D). In most cases, the sum of the percentages of LMX1A-, NKX6-1-, and PAX6-positive cells was <100%. This result suggests that some cells were differentiated outside of the midbrain.

We reconsidered the observed inherent WNT activity (Figure 4G) as it can antagonize not only neuroectoderm differentiation (Blauwkamp et al., 2012) but also affect the AP axis coordinates of induced cells (Kim et al., 2021). We then added a WNT inhibitor concurrently with dual SMAD inhibition during the first 72 h of differentiation (Figure 5A). The transient upregulation of *NPTX1*, an essential event for human neural induction (Boles et al., 2014), was more pronounced in the presence of the WNT inhibitor (Figure 5B). Moreover, the early neuroectodermal/forebrain differentiation was enhanced as indicated by *POU3F1* and *SIX3* (Metzis et al., 2018) (Figure 5B).

AP patterning during mammalian neural development occurs coincidentally with neural specification, followed by DV patterning (Sagner et al., 2021). In our current protocol, ventralizing signals precede AP patterning (Figure S6A) (Steinbeck et al., 2015). Therefore, we decided to retard the timing of adding the ventralizing factor (Figure 5A). When SHH and Purmorphamine were added on day 3, although FOXA2 was equally expressed (Figure 5C), we observed decreases in NKX6-1 and PAX6 off-target cells and the associated increase in LMX1A cells (Figures 5E and S6C; Table S1). This new protocol allowed a thorough induction of 1T47 to the ventral midbrain region (Figures 5E and 5G; Table S1).

We further differentiated the default-elite clones using the improved protocol. The differentiation efficiencies in the midbrain region for the clones 6T9 and 6T20 were exceedingly high but more variable than for 1T47, and the clones 6C4 and 6C6 showed subtotal differentiation efficiencies (Figures 5F and 5G; Table S1). These variations in differentiation efficiencies beyond the initial default neural induction of the default-elite clones signify that the differentiation defectiveness of hPSCs can manifest at a later neuronal differentiation stage.

The high differentiation efficiencies achieved in this study encouraged us to determine whether these progenitors could mature into mDA progenitors/neurons. We investigated the differentiation efficiencies of cells positive for NR4A2 (also known as NURR1), which is a definitive marker of mDA progenitors/neurons (Arenas et al., 2015), using the differentiation-elite clone 1T47 (Figure 6A). The percentage of NURR1-positive cells was 56.5% ± 5.22% on day 29 but progressed to exceedingly high efficiency of 85.0% ± 5.23% on day 42. Furthermore, we noticed that the dendrites of the neurons derived from T-iPSCs were more elaborate than those from C-iPSCs (Figures 6B and 6C). Although the sample size is limited in our study, our data are coherent with the idea that the inherent bias for extraembryonic lineages (Figure 4F) negatively affects the precise spatiotemporal control of the coordinates of differentiation (FOXA2 and LMX1A) and neural maturation (MAP2) (Figures 5C, 5D, 5F, 5G, and 6C).

DISCUSSION

We propose our novel pipeline for the production and quality-controlled selection of T-iPSCs with enhanced differentiation capabilities and indicate that the lack of TET1 activity is a significant cause of the insufficient differentiation potentials of hiPSCs. With the conventional reprogramming regime, we observed fewer epithelialized cells than T-iPSCs (Figure 1D), as acknowledged by the role of TET1 in MET during mouse reprogramming (Li et al., 2010). Our single-cell transcriptome analyses further revealed that the 1T47 T-iPSC clone with a minimum extraembryonic gene signature not only expressed *TET1* uniformly but also exhibited epithelialized colony growth (Figure 4E). Strikingly, this clone exhibited near-complete differentiation toward ventral mDA neurons (Figure 5; Table S1). We attributed the heterogeneous differentiation capabilities among hiPSCs to the metastabilities between the

epiblast cells (somatic precursors) and the extraembryonic-like cells (non-somatic cells). The idea that somatic versus extraembryonic biases may be the source of differentiation inconsistencies is in sharp contrast to the prevailing idea that differentiation propensities are exhibited among the three germ lineages of somatic differentiation (Osafune et al., 2008; Shao et al., 2017), a point that warrants further scrutiny. This study also indicates that bonafide pluripotency-associated genes would be difficult to discern through bulk expression screens as the uniformity of such marker gene expression is cardinal for exerting full pluripotency, as shown here for *TET1* (Figures 4E and 4G).

Organoids, such as brain organoids, have gained popularity in the stem cell field as such methodologies may provide three-dimensional connectivities among PSC-derived cells (Kim et al., 2020; Simunovic and Brivanlou, 2017; Yin et al., 2016). In the case of two-dimensional differentiation, a part of the *in vitro*-induced cells revealed the expression of essential developmental genes in the expression analyses of *in vitro* and *in vivo* counterparts (La Manno et al., 2016; Loh et al., 2016). However, multiple reports chorused that most organoid cells and most induced cells by two-dimensional culture do not reach adequate maturity nor distinguishingly express subtype-specific combinations of genes which are fundamental for the cell's physiological functions (La Manno et al., 2016; Bhaduri et al., 2020). In this study, the dual impacts of our selection procedure of appropriate iPSC clones and the finely tuned differentiation deduced by using such elite clones reach a consensus on the importance of standardization of the pipeline for obtaining target cell types. In the future, it is necessary to investigate whether differentiation-elite T-iPSCs selected by these new stringent selection criteria and the protocol for ventral mDA progenitors accurately represent the pathological model of Parkinson's disease (Bose et al., 2022).

In summary, we developed a new hiPSC induction system with inherent cell-autonomous differentiation screens and showed the quasi-total induction of mDA neurons from T-iPSCs. We incidentally revealed metastability between the late epiblasts and the extraembryonic lineages in multiple iPSC clones, a trait amendable if uniform *TET1* expression was attained. Default-elite T-iPSCs provided differentiation results comparable to, if not better, than those of hESCs. No C-iPSCs could differentiate as efficiently as default-elite T-iPSCs, especially during long-term differentiation. We, therefore, propose the demonstrated T-iPSC-production pipeline as a *de facto* standard for obtaining hPSCs with improved differentiation potentials.

Limitations of the study

A confounding issue in reprogramming is the lack of a direct link between reprogramming factors and the expressivity of their endogenous counterparts. Concerning the episomal delivery of reprogramming factors, such factors are only expressed at earlier stages of reprogramming. Therefore, the expressivity of *TET1* observed among various hiPSC lines, for example, is not a direct output of the expression of the reprogramming vector. However, the endogenous activation of the same genes used for reprogramming is a rule rather than an exception, as seen for *POU5F1* and *SOX2*. Consequently, we could not decipher how the ectopic TET1 instructed the homogeneous endogenous *TET1* expression nor mechanistically conferred differentiation advantages to T-iPSCs. Because complete reprogramming is still a rare event (1 differentiation-elite clone/11 default-elite clones/46 integration-free clones/1,092 epithelialized colonies), a direct assessment of the demethylation events responsible for attaining full pluripotency in the established iPSC clones before differentiation would be highly beneficial. Currently, we are investigating the genome-wide DNA methylation statuses of the C/T-iPSC clones to draw an optimal epigenetic picture for optimum pluripotency of human iPSCs.

ACKNOWLEDGMENTS

We thank Y. Moriyama, Y. Tokuzawa, M. Bagheri, S. Funayama, and H. Kawakami for earlier contributions and technical assistance. This study was supported by Zeon Corporation, SATAKE MultiMix Corporation, Yokogawa Electric Corporation, SyntheticGestalt, and AMED under Grant Number JP20bk0104090. The procedure for T-iPS cell production was filed under patent no. WO2014-069479.

DECLARATION OF INTERESTS

The authors declare no competing interests.

AUTHOR CONTRIBUTIONS

Conceptualization, H. Kato.; Methodology, M. M., K. H-K., and H. Kato.; Formal Analysis, M. M., K. H-K., M. K., and H. Kato.; Investigation, M. M., K. H-K., M. K., and H. Kato.; Writing - Original Draft, M. M., K. H-K., and H. Kato.; Writing - Review & Editing, M. M., K. H-K., M. K., H. Kiyosawa, Y. K., and H. Kato.; Supervision, M. M., Y. K., and H. Kato.; Funding Acquisition, H. Kato.

FIGURE LEGENDS

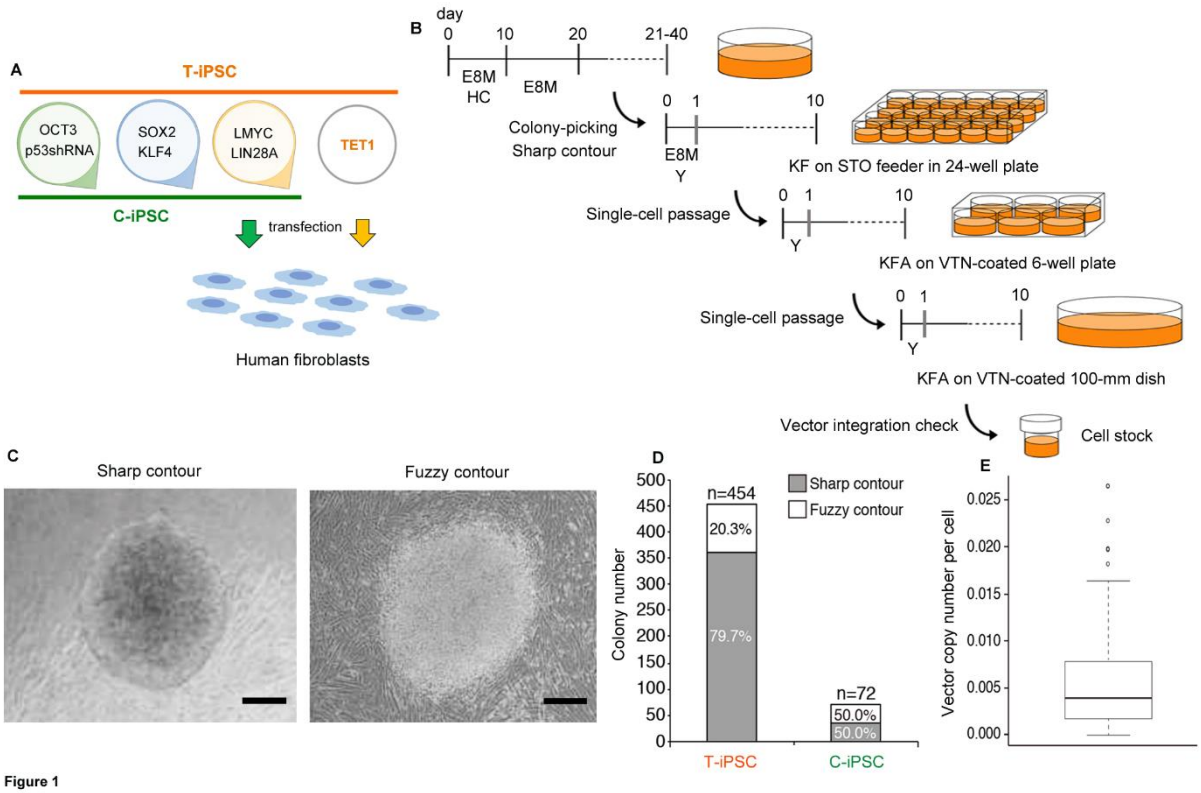

Figure 1. HiPSC production pipelines

(A) Schematic of T-iPSCs and C-iPSCs generation using episomal vectors comprising reprogramming factor cocktail. TET1 vector was used for only T-iPSCs. OCT3 is an alias of POU5F1.

(B) Schematic representation of the timeline and procedure used for hiPSC production. hiPSCs were induced by electroporation of episomal vectors and expanded on STO feeder cells immediately after colony-picking. In the next passage, they were expanded without feeder cells. E8M, Essential 8^{TM} medium. HC, hydrocortisone. Y, Y-27632, a ROCK inhibitor. VTN, vitronectin. The components of STO, KF, and KFA are described in STAR Methods.

(C) Characteristic morphologies of the emerging hiPSCs. Note that the non-reprogrammed fibroblasts served as feeder cells for the hiPSCs. Scale bars, 50 μm.

(D) Bar chart showing the number of T-iPSCs and C-iPSCs colonies (n = 454 T-iPSCs, n = 72 C-iPSCs). The ratio of epithelialized (sharp contour) vs. mesenchymal (fuzzy contour) colonies is depicted in bars for both reprogramming methods.

(E) A boxplot showing copy numbers of integrated reprogramming episomal vectors (n = 46). The box represents the interquartile range, and the midline represents the median.

See also Figure S1.

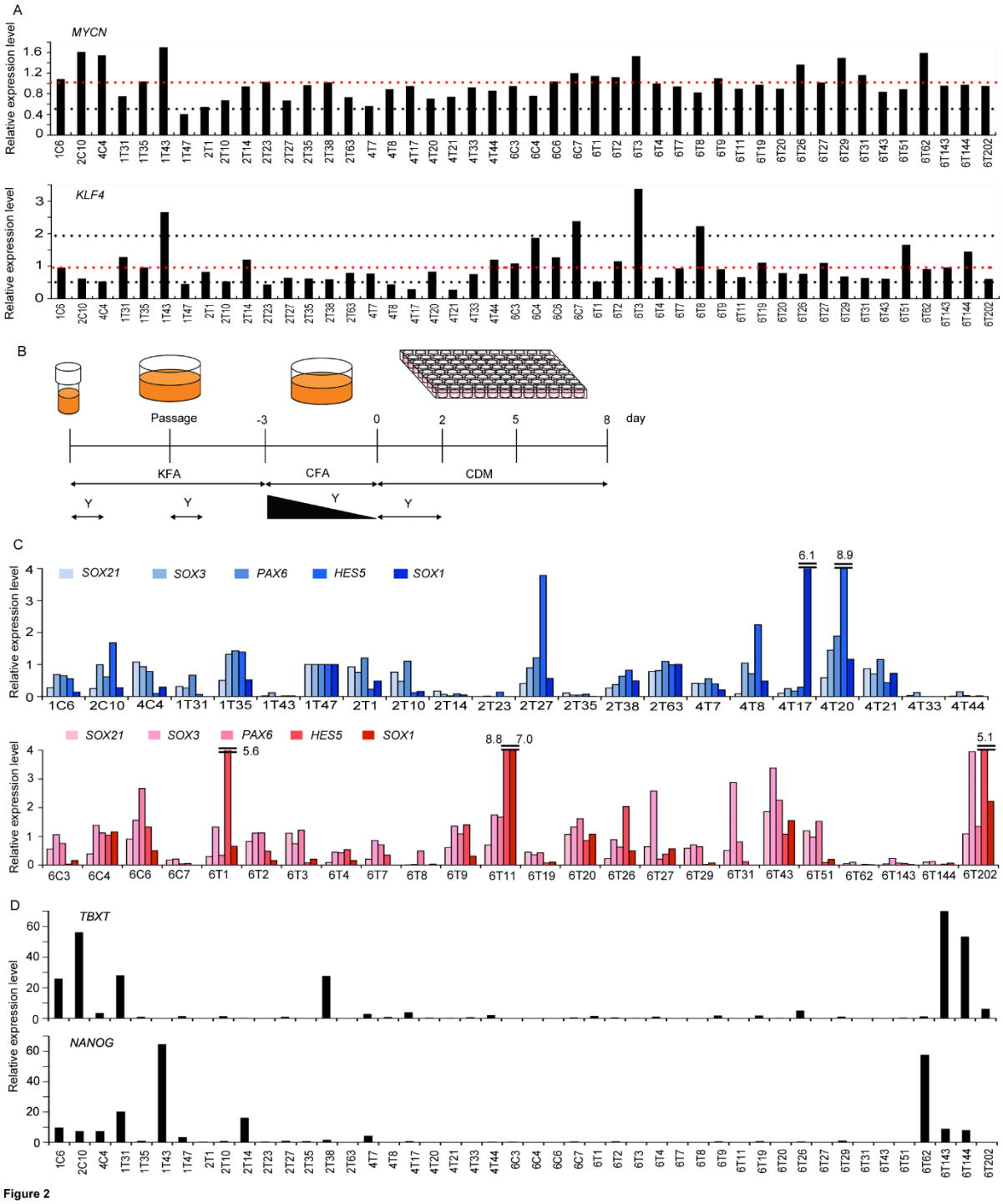

Figure 2

Figure 2. Selection of hiPSC clones by evaluating their inherent default differentiation capability

(A) Expression levels of *MYCN* and *KLF4* for each clone at an undifferentiated state (n = 1). The clone IDs are indicated on the x-axis. The red dotted lines indicate the average expression level, and the black lines indicate half or two times the average expression level.

(B) Schematic representation of the default differentiation timeline and procedure used to evaluate the differentiation capabilities of T/C-iPSC clones. Spheres were generated on v-bottom 96-well plates in CDM and Y, Y-27632, a ROCK inhibitor. The components of KFA, CFA, and CDM are described in STAR Methods.

(C) The relative expression levels of neural markers on day 8 in male (c, top panel) and female (c, bottom panel) hiPSCs. The clone IDs are indicated on the x-axis. Expression levels were normalized to those of clone 1T47 (n = 1).

(D) The relative expression levels of *TBXT* (top) and *NANOG* (bottom) on day 8 (n = 1). The clone IDs are indicated on the x-axis.

See also Figures S2, S3, and S4.

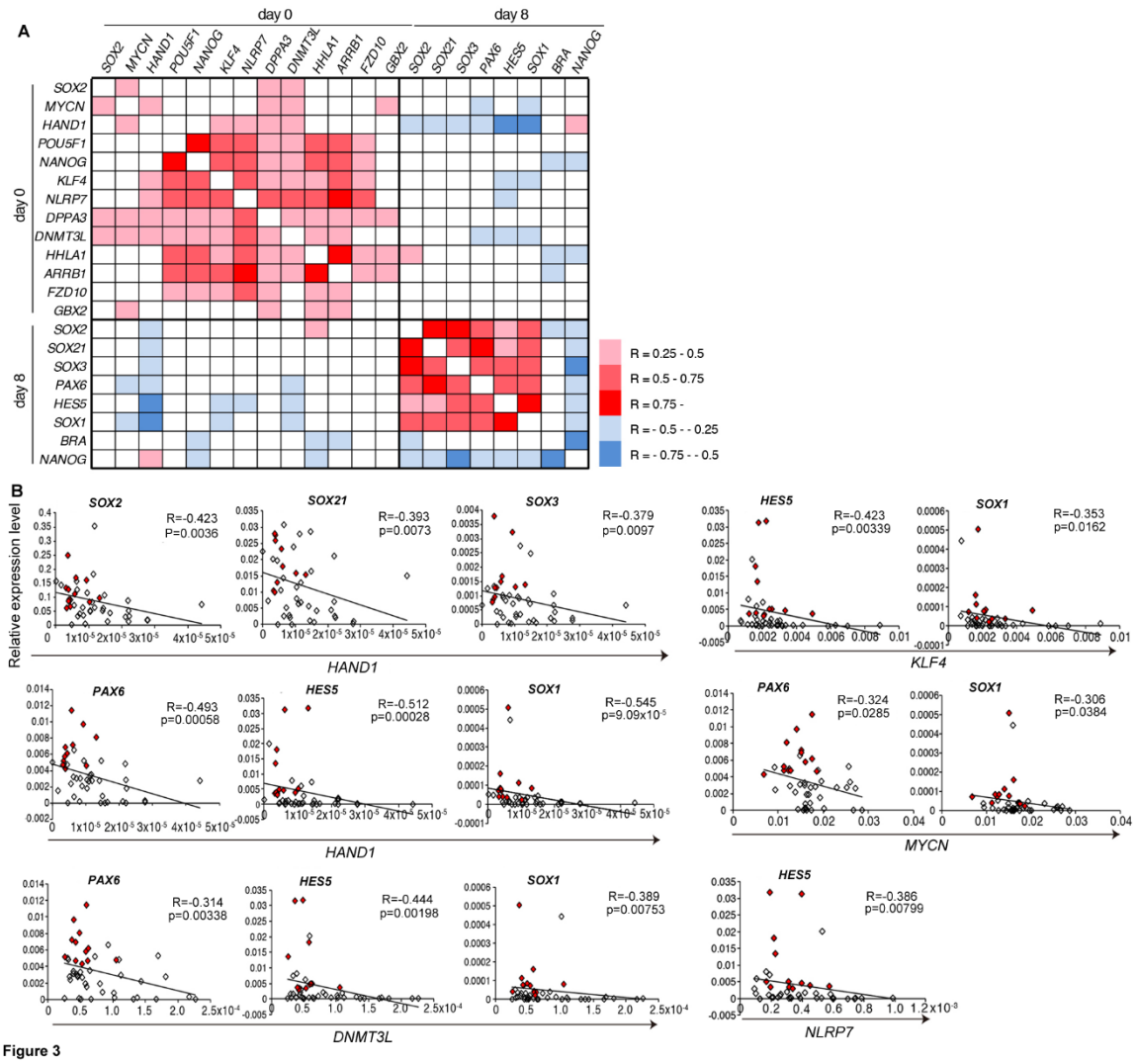

Figure 3. A selected battery of genes predicting the differentiation refractoriness of hiPSCs

(A) Correlation matrix for marker expression levels and the default differentiation behaviors of all vector-free hiPSC clones. The colored boxes indicate all significant correlations ($P < 0.05$) between the two markers. A red box indicates a positive correlation, whereas a blue box indicates a negative correlation. Color intensity shows correlation strength (R).

(B) Scatter plots showing the relative gene expression levels of the neural markers on differentiation day 8 (y-axis) versus the levels of the selected differentiation-resistant markers (Cacchiarelli et al., 2015) (x-axis). The red dots indicate the default-elite clones (A, B**,** total

clone number = 46). The *GAPDH*-normalized expression levels for each gene are shown on both axes.

See also Figure S5.

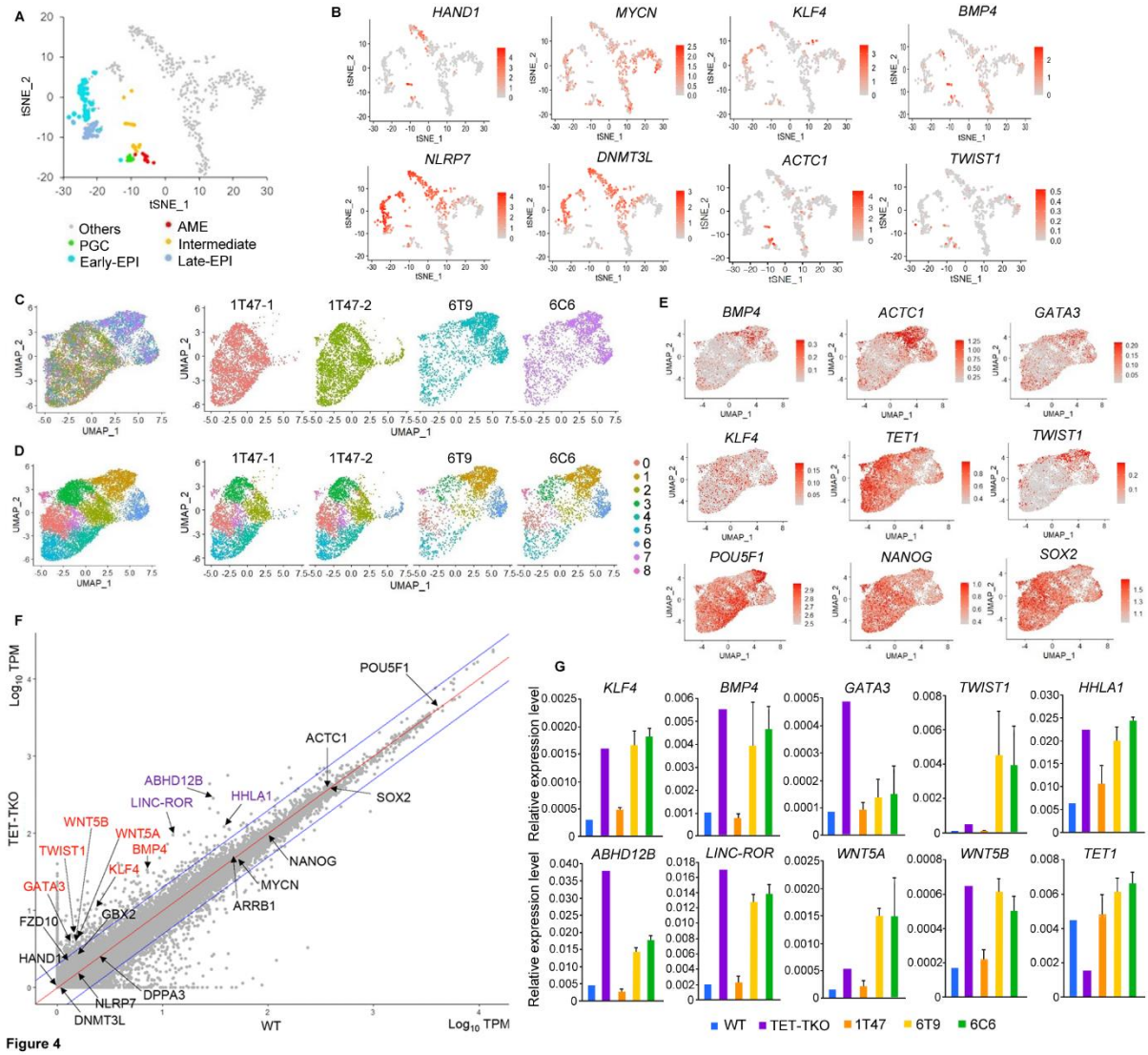

Figure 4. Single-cell and bulk RNA-seq analyses of cultured human early embryo cells, the representative elite hiPSCs, hESCs, and TET-TKO cells.

(A) The t-SNE plot of the single-cell RNA profiles of early human embryos (Xiang et al., 2020). Each dot depicts a single cell, and six clusters were marked with different colors at specific stages, such as early-EPI (early-epiblast, light blue), late-EPI (late-epiblast, dark

blue), PGC (primordial germ cell, green), AME (amnion, red), intermediate (yellow), and others (gray). “Others” represent trophoblast-derived cells.

(B) The gene expression of differentiation-resistance markers, AME markers, *ACTC1* and *BMP4*, and the epithelial-mesenchymal transition marker, *TWIST1*, was visualized using feature plots.

(C) UMAP plot for the representative elite hiPSCs. Each dot depicts a single cell. Left panel: the merged UMAP plot for the four cell samples. Right panel: individual clone contributions to the merged UMAP plot in the left panel. 1T47-1 and 1T47-2 are technical duplicates.

(D) UMAP plots and annotated functional clusters. Eight clusters were identified and marked with different colors. Left panel: the merged UMAP plot for the four cell samples. Right panel: individual clone contributions to the merged UMAP plot in the left panel.

(E) The gene expression of *TET1*, *POU5F1*, *SOX2*, *NANOG,* and AME markers in the integrated analysis is visualized using feature plots.

(F) Correlation of gene expression (measured by RNA-seq) between wild-type HUES8 cells (WT) and TET1, TET2, and TET3 triple-knockout (TET-TKO) ones (Charlton et al., 2020). The genes marked in purple were previously described as differentiation-resistant markers (Koyanagi-Aoi et al., 2013). Genes marked in red represent extraembryonic markers with more than two-fold differences between WT and TET-TKO.

(G) The relative expression levels of *TET1*, differentiation-resistance markers, and AME markers in each cell line. The values for 1T47, 6T9, and 6C6 are the mean ± standard deviation (n = 3). HiPSC clones were analyzed at passages P17, P27, and P18 (1T47), P24, P28 and P29 (6T9), P21, P25, and P26 (6C6). Expression levels were normalized against those of *GAPDH*.

See also Figure S5.

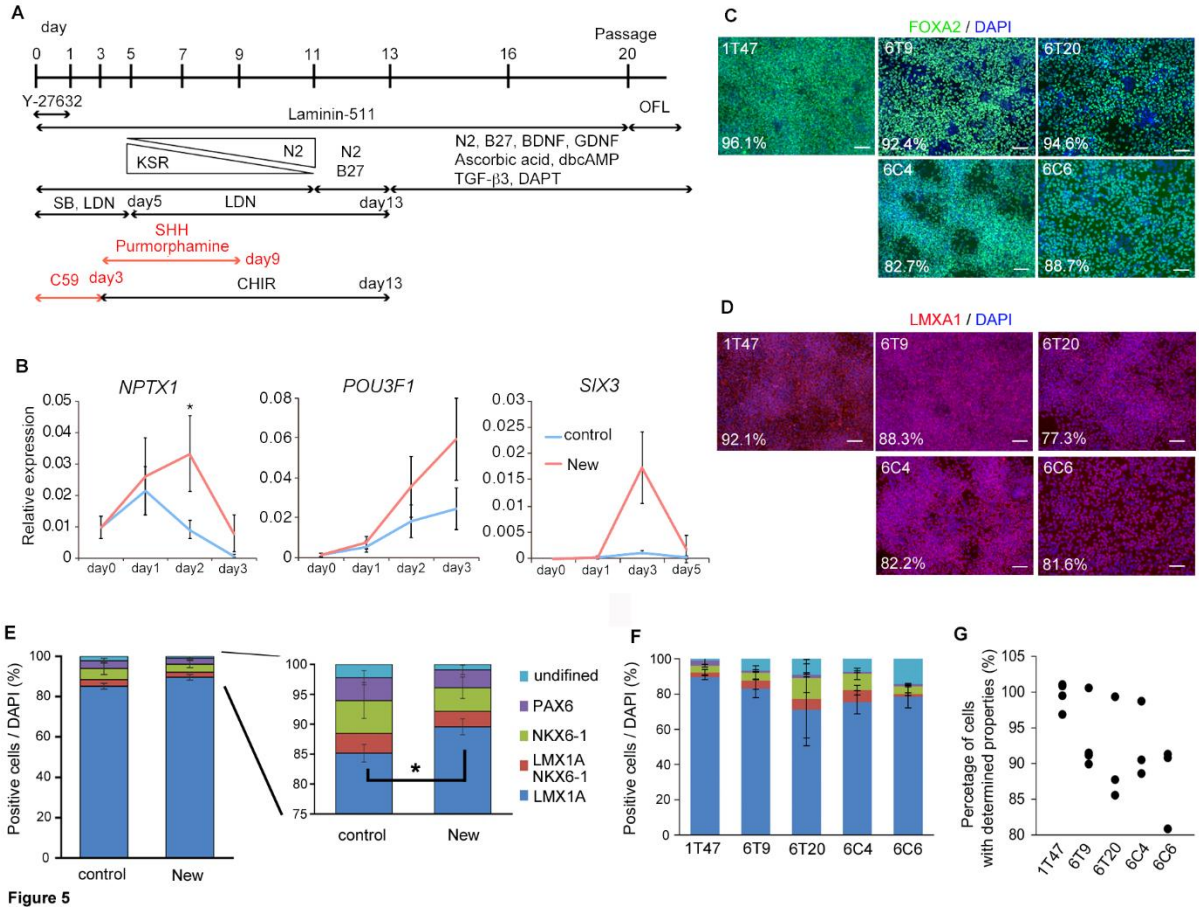

Figure 5. Improved ventral mDA neuron differentiation

(A) Schematic representation of improved mDA neuron differentiation. SB, SB431542; LDN, LDN193189; CHIR, CHIR99021; C59 WNT-C59; OFL, ornithine, fibronectin, and Laminin (iMatrix-511). KSR-media were gradually changed to N2-media from day 5 to day 11.

(B) The relative expression levels of neuroectodermal and forebrain markers at an early stage of differentiation. Control (original protocol, blue line; as shown in Figure S6A) and New (new protocol, red line) (n = 3). The error bars represent the mean ± standard deviation. * $P < 0.05$.

(C and D) Representative immunostaining data with DAPI (blue) and (C) FOXA2 (green) or (D) LMX1A (red) on day 19 in default-elite clones. The percentages indicate the ratio of each positive cell type. The values are represented as the mean (C; n = 2-3, D; n = 3). Scale bars, 50 μm.

(E and F) Bar plots showing the ratio of the ventral or lateral midbrain regions on day 19 for clone 1T47 (E, F) and other default-elite clones (F) (n = 3). The data are presented as the mean ± standard deviation.

(G) Bar plots showing the sum of all ratios of cells expressing ventral midbrain regional markers on day 19 (n = 3). Y axis starts from 80% to show details of the minor populations. See also Figures S6 and S7.

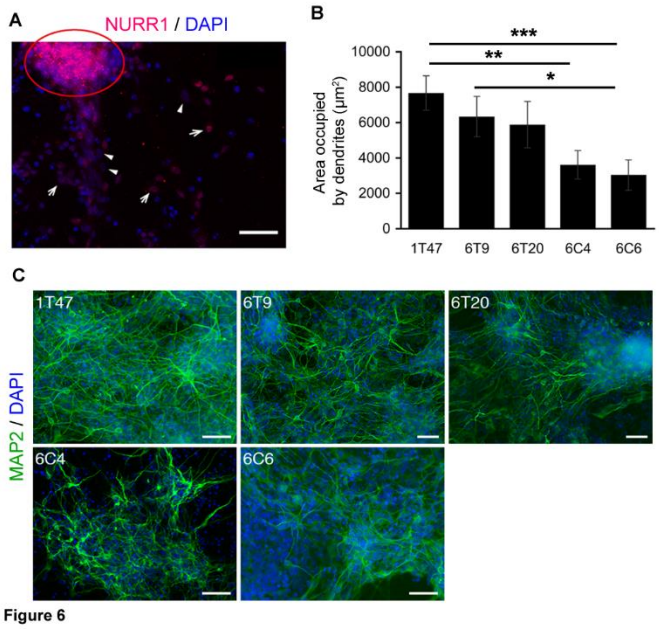

Figure 6. Enhanced directed differentiation and maturation of default-elite C/T-iPSCs to mDA neurons

(A) 1T47-derived NURR1-positive mDA neurons on day 29 (arrows, NURR1-positive neurons; arrowheads, NURR1-negative neurons; the cells in sphere-like aggregates encircled in red were not counted).

(B and C) Morphological evaluation of MAP2-positive cells on day 29. The values are presented as the mean ± standard deviation. Scale bars, 50 μm. The clone names are indicated on the x-axis. One-way analysis of variance and Tukey's multiple-comparison tests were

performed to determine the significance of the observed differences (B). * $P < 0.05$, ** $P < 0.01$, *** $P < 0.001$. n = 3.

STAR METHODS

Resource Availability

Lead contact

Requests for further information should be directed to and will be fulfilled by the lead contact, Hidemasa Kato (hidemasa.kato.zz@ehime-u.ac.jp)

Materials availability

Requests for resources and reagents should be directed to and will be fulfilled by the Lead Contact, Hidemasa Kato (hidemasa.kato.zz@ehime-u.ac.jp)

Data and code availability

The accession number for the single-cell RNA-seq data generated in the present study is DRA013769 (DNA Data Bank of Japan [DDBJ]).

EXPERIMENTAL MODEL AND SUBJECT DETAILS

hiPSC induction and culture

Human fibroblasts (from male neonatal foreskin, 106-05N; female fetal fibroblasts, 106-05F) were purchased from Cell Applications Inc. and cultured in Dulbecco's modified Eagle's medium (DMEM; Nacalai Tesque) supplemented with 10% fetal bovine serum (FBS; Hyclone), 100 µg/mL L-ascorbic acid 2-phosphate trisodium salt (FUJIFILM Wako), and 1× penicillin/streptomycin (P/S; Gibco). HiPSCs were induced by applying a previously reported method using episomal vectors (Yu et al., 2009). Episomal vectors (pCXLE-hOCT3/4-shp53-F: 27077, pCXLE-hSK: 27078, and pCXLE-hUL: 27080) were obtained from Addgene. To establish the T-iPSCs, a TET1 episomal vector (comprising complementary DNA encoding

the human *TET1* open-reading frame, cloned into the pCXLE vector) was used to top the three episomal vectors upon reprogramming. The cells were transfected using the Human Dermal Fibroblast Nucleofection® Kit (Amaxa Biosystems [Lonza]) and Nucleofector™ 2B apparatus (Amaxa Biosystems [Lonza]) according to the manufacturer's instructions. Approximately 1×10^6 low-passage fibroblasts and 1 μg of each vector were used per transfection, and the cells were plated immediately in a human fibroblast medium after electroporation. The following day, the culture medium was replaced with Essential 8™ Medium (E8M; Gibco) supplemented with 100 nM hydrocortisone (Sigma-Aldrich) and 1× P/S. The medium was changed every other day. E8M, which contains TGF-β, was chosen due to its potentiating effect of activating SMAD2/3 during reprogramming (Ruetz et al., 2017). The medium was changed every other day. From day 10 of iPSC induction, E8M without hydrocortisone was used. The iPSC colonies with sharp contours were picked up, triturated into E8M supplemented with 10 μM Y-27632 (FUJIFILM Wako), and plated onto STO feeder cells treated with mitomycin C (FUJIFILM Wako). The culture medium was replaced the next day with KnockOut™ DMEM/F12 (Thermo Fisher Scientific) supplemented with 20% KnockOut™ Serum Replacement (KSR; Gibco), 2 mM GlutaMAX™-I (Gibco), 1× MEM non-essential amino acids (NEAA, Gibco), 0.1 mM β-mercaptoethanol (2-ME, FUJIFILM Wako), 5 ng/mL basic fibroblast growth factor (bFGF, Peprotech), 5 mM NaOH (FUJIFILM Wako), and 1× P/S (KF medium). After the colonies had been selected, the medium was changed daily. When the iPSC colonies grew, they were dissociated with 0.01% trypsin/0.1 mM EDTA buffer (trypsin/EDTA; Nacalai Tesque) and plated onto 5 ng/mL vitronectin (Invitrogen)-coated 6-well plates in KnockOut™ DMEM/F12 supplemented with 20% KSR, 2 mM GlutaMAX™-I, 1×NEAA, 0.1 mM 2-ME, 15 ng/mL bFGF, 10 ng/mL activin A (R&D Systems), 5 mM NaOH, and 1× P/S (KFA medium) supplemented with 10 μM Y-27632. The culture medium was then replaced daily with the KFA medium without Y-27632. The KFA

medium was routinely used for the expansion and maintenance of hiPSCs throughout this study. The clones were further subcultured in a 100-mm dish (Becton Dickinson) until a confluent state had been reached. Half the cells were cryopreserved in a cell stock solution composed of 10% dimethylsulfoxide (Nacalai Tesque) and 90% FBS. Genomic DNA was obtained from the remaining cells to analyze the genomic integration of the plasmid vectors. HiPSCs were dissociated in trypsin/EDTA for feeder-free culture and replated in the KFA medium containing 10 μM Y-27632. Twenty-four hours after each passage, the medium was replaced with KFA medium lacking Y-27632. The hiPSCs were passaged at 80–90% confluence every 3 or 4 days. On average, it took 28 days for the colonies to form and 17 days for the iPSC clones to be expanded sufficiently to prepare frozen stocks (and hence "established").

Evaluating the differentiation capabilities of hiPSCs by default differentiation

Pilot experiments using hiPSCs and attempts to derive neural cells from monkey ESCs (Ono et al., 2014) revealed that KSR-containing culture media were incompatible with default differentiation (data not shown). Therefore, we gradually changed the KSR-media to a chemically defined medium (CDM) before differentiation to facilitate the efficient derivation of neural cells (Ono et al., 2014). KFA-cultured hiPSCs were dissociated with trypsin/EDTA, and 1×10^6 cells were replated onto a vitronectin-coated 100 mm dish in CDM supplemented with 10 ng/mL bFGF, 2 ng/mL activin A, 3% KSR, and 10 μM Y-27632 (CFA). CDM is composed of Iscove's modified Dulbecco's medium/F-12 (Thermo Fisher Scientific), 2 mM GlutaMAX^{TM}-I, 7 μg/ml Insulin (FUJIFILM Wako), 15 μg/ml transferrin (Sigma-Aldrich), 450 μM monothioglycerol (Sigma-Aldrich), 1× lipid concentrate (Gibco), 5 mg/ml bovine serum albumin fraction V (Sigma-Aldrich), 200 μM L-ascorbic acid 2-phosphate trisodium salt, 0.1 mM NEAA, 80 nM sodium selenite (Sigma-Aldrich), and 1× P/S. Half the media was

carefully replaced with CFA without Y-27632 daily. On the third day of replication, the cells were dissociated with trypsin/EDTA and plated at 500 cells per well in a 96-well low-binding Sphera plate (NUNC, Thermo Fisher Scientific) in 150 μL of CDM supplemented with 10 μM Y-27632. The day the cells were seeded was designated as differentiation day 0. Two days after seeding (day 2), 100 μL of the medium was removed to avoid aspiration of the spheres, and 150 μL of fresh CDM without Y-27632 was added. On differentiation day 5, 100 μL of the medium was removed, and 100 μL of fresh CDM was added. On differentiation day 8, the induced aggregates were collected.

Differentiation of extraembryonic lineage cells

Differentiation of extraembryonic lineage cells was performed based on the previous report (Zheng et al., 2019). KFA-cultured hiPSCs were dissociated with trypsin/EDTA, and 2×10^5 cells were replated onto a vitronectin-coated 6-well plate in a differentiation medium composed of KnockOut™ DMEM/F12 supplemented with 20% KSR, 2 mM GlutaMAX™-I, 1× NEAA, 0.1 mM 2-ME, 50 ng/mL BMP4 (R&D systems), 10 ng/mL activin A, 5 mM NaOH, 1× P/S, and 10 μM Y-27632. The differentiation medium without Y-27632 was changed every day. On differentiation day 4, the cells were collected and their RNAs were extracted.

Differentiation of ventral midbrain neural progenitor cells

Three different media were used to induce ventral midbrain neural progenitors. The first medium tested was a differentiation medium (DM), which was composed of DMEM (Nacalai Tesque), 15% KSR, 2 mM GlutaMAX™-I, 1 mM sodium pyruvate (Sigma-Aldrich), 10 μM 2-ME, and 0.1× P/S. The second medium tested was N2 medium (N2M), which was composed of DMEM/F12 (FUJIFILM Wako), 1× N-2 Supplement (Gibco), 2 mM

GlutaMAX™-I, and 0.1× P/S. The third medium tested was the neural induction medium (NIM), composed of 50% N2M and 50% NB27. NB27 comprised neurobasal medium (Gibco), 1× B-27™ Supplement (Gibco), 2 mM GlutaMAX™-I, and 0.1× P/S. Default-elite or non-default-elite cell lines were cultured in KFA medium and subcultured two or three times. The cells were dissociated with trypsin/EDTA, and 1.5×10^5 cells/cm^2 were seeded onto plates coated with 0.5 μg/cm^2 iMatrix-511 (Nippi) in DM supplemented with 10 μM Y-27632, 100 nM LDN193189 (LDN; Sigma-Aldrich), 10 μM SB431542 (SB; Sigma-Aldrich), and 10 nM WNT-C59 (C59; Cellagen Technology). The day that the cells were seeded was designated as differentiation day 0. On the following day (day 1), the medium was changed to DM supplemented with LDN, SB, and C59. On differentiation days 5, 7, and 9, the medium was changed to 75% DM and 25% N2M, 50% DM and 50% N2M, or 25% DM and 75% N2M, respectively. On differentiation day 11, the medium was changed to N2M supplemented with 0.5× B27. LDN was added daily to the medium from day 0 to 11, SB from day 0 to 4, and C59 from day 0 to 2. Ventralization was initiated by adding 100 ng/mL Sonic Hedgehog C24II (R&D Systems) and 2 μM purmorphamine (FUJIFILM Wako) from day 3 to 8. 3 μM CHIR99021 (Sigma-Aldrich) was added to the medium from day 3 to 12. Beginning on differentiation day 13, the medium was changed to NIM supplemented with 10 ng/mL BDNF (FUJIFILM Wako), 10 ng/mL GDNF (FUJIFILM Wako), 1 ng/mL TGF-β3 (R&D Systems), 200 μM L-ascorbic acid 2-phosphate trisodium salt, 200 μM N6,2-O-dibutyryladenosine 3, 5-cyclic monophosphate (Sigma-Aldrich), and 5 μM DAPT (Tocris Bioscience). For immunostaining, the cells were dissociated with Accumax (Innovative Cell Technologies, Inc). Then, 4×10^5 cells/cm^2 were seeded onto culture slides (BD Biosciences) coated with 15 μg/mL poly-l-ornithine (Sigma-Aldrich), 2 μg/mL fibronectin (Sigma-Aldrich), and 0.5 μg/cm^2 iMatrix-511 in NIM supplemented with the above growth factors and 10 μM Y-27632.

The medium was changed every day from day 0 to 16, and half of the medium was changed every 2 or 3 days from day 17 onward.

METHOD DETAILS

Immunofluorescence of the differentiated cells

On days 19, 29, and 42, individual induced cells were fixed in 4% paraformaldehyde (FUJIFILM Wako), washed, and preserved in phosphate-buffered saline (PBS; TaKaRa) at 4 °C until use. They were blocked in 5% (v/v) normal donkey serum (NDS; Millipore)/0.3% (v/v) Triton X-100 (Nacalai Tesque)/PBS for 1 h. Primary antibodies were diluted in 1% NDS/0.3% Triton X-100/PBS and incubated overnight at 4 °C. The samples were then washed in 0.05% (v/v) Tween-20 (Sigma-Aldrich)/PBS and incubated with secondary antibodies in 1% NDS/0.3% Triton X-100/PBS for 2 h, followed by washing with 0.05% Tween-20/PBS and incubation with DAPI (Invitrogen) in 1% NDS/0.3% Triton X-100/PBS for 10 min. Finally, the samples were washed with 0.05% Tween-20/PBS and mounted with an anti-photobleaching mounting medium comprising 2.4 g Mowiol (Millipore), 6 mL glycerol (FUJIFILM Wako), 6 mL distilled water, 12 mL 200 mM Tris-HCl (Nacalai Tesque), and 0.66 g of 1.4-diazabicycle (2.2.2) octane (Sigma-Aldrich). For immunofluorescence, we used primary antibodies against LMX1A (1:1000; Millipore), PAX6 (1:500; BD Biosciences), MAP2 (1:2000; Sigma-Aldrich), beta-tubulin 3 (TuJ1, 1:2000; Covance), NKX6-1 (1:1000; R&D Systems), NR4A2 (NURR1) (1:1000; Santa Cruz Biotechnology), and FOXA2 (1:500; R&D Systems). Alexa Fluor™-conjugated antibodies (1:500, Invitrogen) were used as secondary antibodies. Given the fluorescence filter constraints, we could not simultaneously perform three-color immunostaining and nuclear staining. Therefore, we individually stained cells for LMX1A and NKX6-1, or NKX6-1 and PAX6, and counted approximately 3000 cells in three randomly selected fields to determine the ratios of cells positive for the respective

markers using the ImageJ software. In serial sections, immunostaining for LMX1A and PAX6 revealed very few double-positive cells for both markers (data not shown). The stained cells were imaged using a Biorevo BZ-9000 fluorescence microscope (Keyence).

PCR and qPCR analyses of integrated episomal vectors

Genomic DNA (gDNA) was extracted using the DNeasy Blood & Tissue Kit (QIAGEN). Conventional (semi-quantitative) PCR was performed using Ex Taq DNA polymerase (TaKaRa). qPCR was performed using Thunderbird SYBR qPCR Mix (Toyobo). The cycle threshold (Ct) values for the episomal vector were normalized against gDNA (measured using the CFTR primer set). The primer sequences for gDNA detection are listed in Table S2. The pEP4-SF1 and pEP4-SR1 primers (Table S2) were used to detect the episomal vector backbones for semi-quantitative PCR (International Stem Cell et al., 2007). For qPCR, the pEP4-SR1 primer was replaced with an in-house designed pEP4-SR3 (Table S2). Genomic DNA (50 or 20 ng) was used as a template for conventional PCR or qPCR, respectively. gDNA extracted from male human dermal fibroblasts was used as a negative control.

Quantitative PCR analysis of differentiated cells

Total RNA was purified from the samples using the RNeasy Plus Mini Kit (QIAGEN). Over 50 ng of total RNA was reverse-transcribed using ReverTra Ace (Toyobo) and oligo-dT primers (Toyobo). The qPCR analysis was conducted using Thunderbird SYBR qPCR Mix (Toyobo) and a Thermal Cycler Dice Real Time System (Bio-Rad). The following thermocycling conditions were used for qPCR: 95ºC for 30 sec, 45 cycles of 95ºC for 5 sec, and 60ºC for 30 sec. The data were assessed using the ΔΔCt method and normalized to glyceraldehyde-3-phosphate dehydrogenase (*GAPDH*) expression. Error bars represent the

standard deviation of 3 biological replicates. The sequences of the primers used for qPCR are listed in Table S2.

Isolation and RNA-sequencing of single cells

Single-cell RNA-sequencing (scRNA-seq) was performed using the 10× Chromium platform using the Single-Cell 3′ reagent kits v3 Chemistry according to the manufacturer's protocol (10× Genomics). Libraries were sequenced on a DNBSEQ-G400 (MGI) with paired-end sequencing. Reads were aligned to the human reference genome (GRCh38/hg38) using the STARsolo package of STAR software (version 2.7.6a) (Dobin et al., 2013). The integration analysis was performed using the Seurat package in R v4.0.0 (Butler et al., 2018). The Seurat package was also used for normalization, variable gene identification, anchor identification, scaling, linear dimensional reduction, and clustering analysis (dims = 1:30). Nonlinear dimensional reduction analysis (UMAP) was performed using the RunUMAP function (dims = 1:30) in the Seurat package. Gene expression profiles were visualized on a UMAP plot using the FeaturePlot function (*BMP4*, *ACTC1*, *GATA3*, *TWIST*, *SOX2*, and *TET1*) or the RNA assay function (*POU5F1* and *NANOG*) in the Seurat package.

RNA-seq processing

RNA-seq data analyses were performed for 1T47, 6T9, and 6C6 clones cultured in an undifferentiated culture condition (KFA medium). Total RNA was purified using miRNeasy Mini Kit (QIAGEN) according to the manufacturer's protocol. RNA-seq libraries were prepared using the TruSeq Stranded Total RNA LT Sample Prep Kit with Ribo-Zero Human/Mouse/Rat (Illumina). We generated biological triplicate data for 1T47, 6T9, and 6C6 clones by harvesting cells at different passage numbers. The RNA-seq libraries were sequenced on the Illumina Novaseq 6000.

hiPSC karyotyping

Nihon Gene Research Laboratories, Inc. karyotyped the T/C-iPSC lines by performing Giemsa testing.

Quantification and Statistical Analysis

Correlation data analysis

Statistical analyses were performed using the R statistical software package. We used Pearson's test for correlation analyses when the expression values followed a normal distribution; otherwise, Spearman's test was used. The Shapiro–Wilk test was used to assess normal distributions. A two-sample *t*-test was used for comparisons between the two groups. Probability values < 5% were considered to reflect statistically significant differences.

Reanalysis of published scRNA-seq data

scRNA-seq data from cultured human early embryos (6 to 14 days post-fertilization) were downloaded from the Gene Expression Omnibus database (GSE136447) (Xiang et al., 2020). Reads were aligned to the human reference genome (GRCh38/hg38) using the STARsolo package of STAR software (Dobin et al., 2013). The Seurat package in R software was used for normalization, variable gene identification, scaling, linear dimensional reduction, and clustering analysis (dims = 1:20 and resolution = 0.5). The 1483 most variable genes in 552 cells were selected. Nonlinear dimensional reduction analysis (t-SNE) was performed using the RunTSNE function (dims = 1:20) in the Seurat package. Gene expression profiles were visualized on a t-SNE plot using the FeaturePlot function in the Seurat package. We adhered to the annotations of most cell lineages in the original article with a few modifications. Pre-EPI (Epiblast) and Post-EPI were renamed to early-EPI and late-EPI, respectively, based on

the expression of the naïve markers, *Sushi domain containing 2* (*SUSD2*) and *KLF17*, which demarcate early-EPI. PSA-EPI was renamed PGC as these cells express primordial germ cell markers, such as *PR/SET domain 14* (*PRDM14*).

RNA-seq Data Analysis

RNA-seq reads were aligned to the human reference genome (GRCh38/hg38) using the STAR aligner v2.7.0a with default parameters (Dobin et al., 2013). The human transcriptome index was generated using the reference genome (GRCh38/hg38) with Ensembl version 95. We calculated the transcripts per million mapped reads (TPM) using RSEM v1.3.1 with default parameters (Li and Dewey, 2011) and considered those as expression levels. HUES8 WT data (SRX5496558) and TET-TKO data (SRX5496559) from Charlton et al. (2020) were re-mapped to the human reference genome (GRCh38/hg38) and analyzed as mentioned above. Expression levels were normalized against those of *GAPDH*.

Evaluating MAP2-positive induced cells

The lengths of the MAP2-positive neurites were measured using ImageJ software. The relative dendrite region was calculated as the average number of dendrites extending from the cell body times the average dendrite length^2. Error bars represent the standard deviation of 3 biological replicates. Statistical significance was determined by a One-way analysis of variance and Tukey's multiple-comparison tests using R software. Significance was determined by $p<0.05$. * $P < 0.05$, ** $P < 0.01$, *** $P < 0.001$.

SUPPLEMENTAL INFORMATION

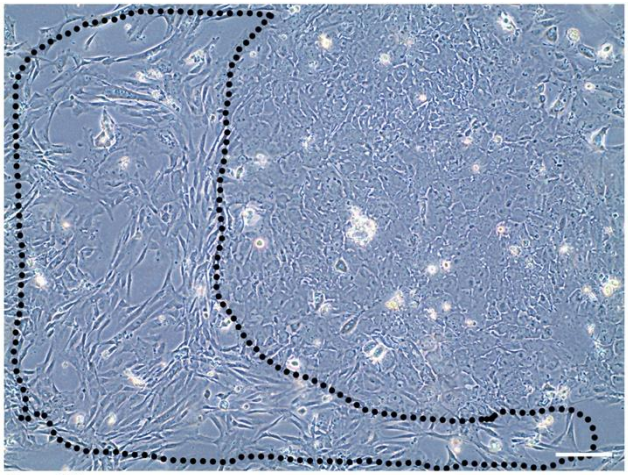

Figure S1

Figure S1 (related to Figure 1)

Figure S1. Mesenchymal revertants during iPSC expansion. A subconfluent culture during the expansion of a picked colony in KFA medium. Note that the cells in the encircled area show a mesenchymal-like morphology. Scale bar, 50 µm.

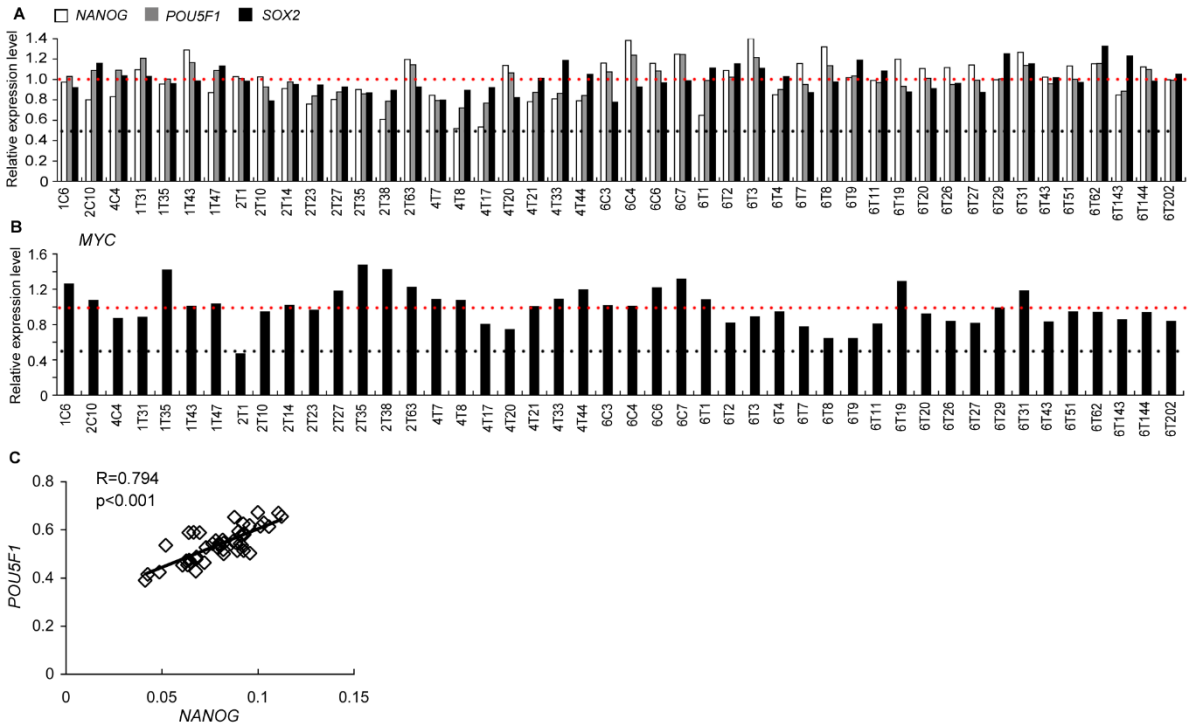

Figure S2

Figure S2 (related to Figure 2)

Figure S2. Pluripotency-associated gene expression and correlations among T/C-iPSCs. (A and B) The relative expression levels of pluripotency-related genes are indicated ([A] white, *NANOG*; gray, *POU5F1*; black, *SOX2*, and [B] *MYC*). The x axis shows the clone names. The red dotted line shows the average expression levels, and the black line indicates half of the average expression level. (C) Relative expression levels of *NANOG* versus *POU5F1* on day 0. Pearson's correlation analysis results are presented as correlation coefficient (R) and p-value.

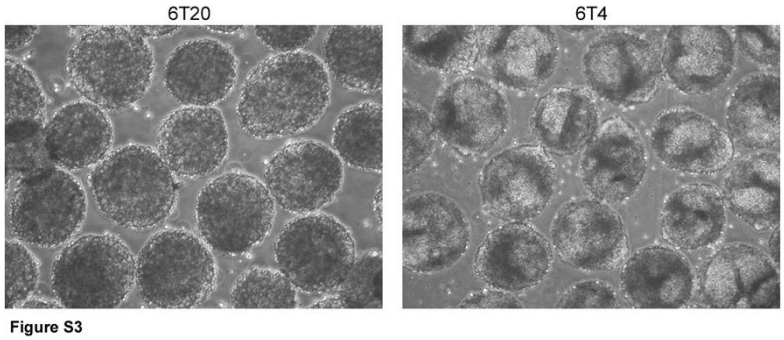

Figure S3 (related to Figure 2)

Figure S3. Morphology of spheroids on day 8 of default differentiation. All clones with high differentiation capabilities formed uniform-sized and dense spheres, such as 6T20 (left panel). Spheres with sac-like structures such as 6T4 (right) exhibited low expression levels of neural markers.

Cell line	Results of Karyotyping
1T35	46, XY [18] ; 47, XY, +X [2]
1T47	46, XY [20]
2T27	46, XY [5] ; 47, XY, +20 [8] ; 47, XY, +X [7]
2T63	47, XY, +X [9] ; 47, XY, +mar [7] ; 47, XY, +20 [4]
4T20	46, XY [7] ; 47, XY, +20 [13]
6T9	46, XX [20]
6T11	46, XX [6] ; 47, XX, +13 [14]
6T20	46, XX [20]
6T43	46, XX [20]
6C4	46, XX [19] ; 46, XX, -18, +mar [1]
6C6	46, XX [20]

Figure S4

Figure S4 (related to Figure 2)

Figure S4. Karyotyping of default-elite clones. The numbers in square brackets represent the number of observed karyotypes among the 20 nuclei counted. +mar, marker chromosome of unknown origin.

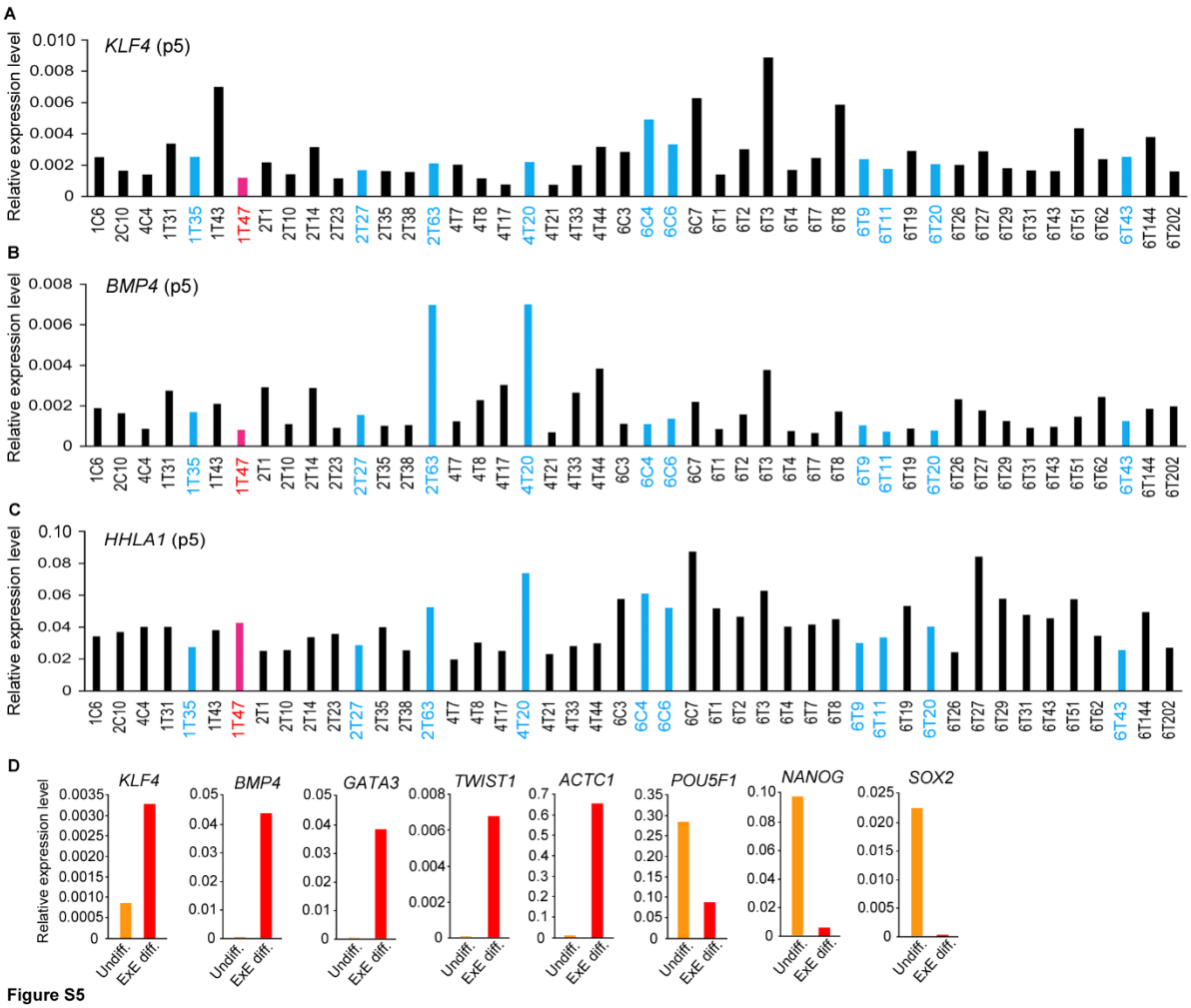

Figure S5 (related to Figure 4)

Figure S5. The expression levels of differentiation-resistant and extraembryonic markers in low-passaged undifferentiated iPSCs and after extraembryonic differentiation. (A, B, and C) The relative expression levels of *KLF4*, *BMP4,* and *HHLA1* in each hiPSCs at passage 5. The differentiation-elite clone, 1T47, is highlighted in red, whereas default-elite clones are in blue. The graph for *KLF4* in Figure 2A was re-posted with slight modifications in line with those of *BMP4* and *HHLA1*. (D) The relative expression levels of pluripotency-related and extraembryonic (ExE) markers in the undifferentiated 1T47 cells (Undiff.) and the BMP4-induced cells (ExE diff.) (n = 1).

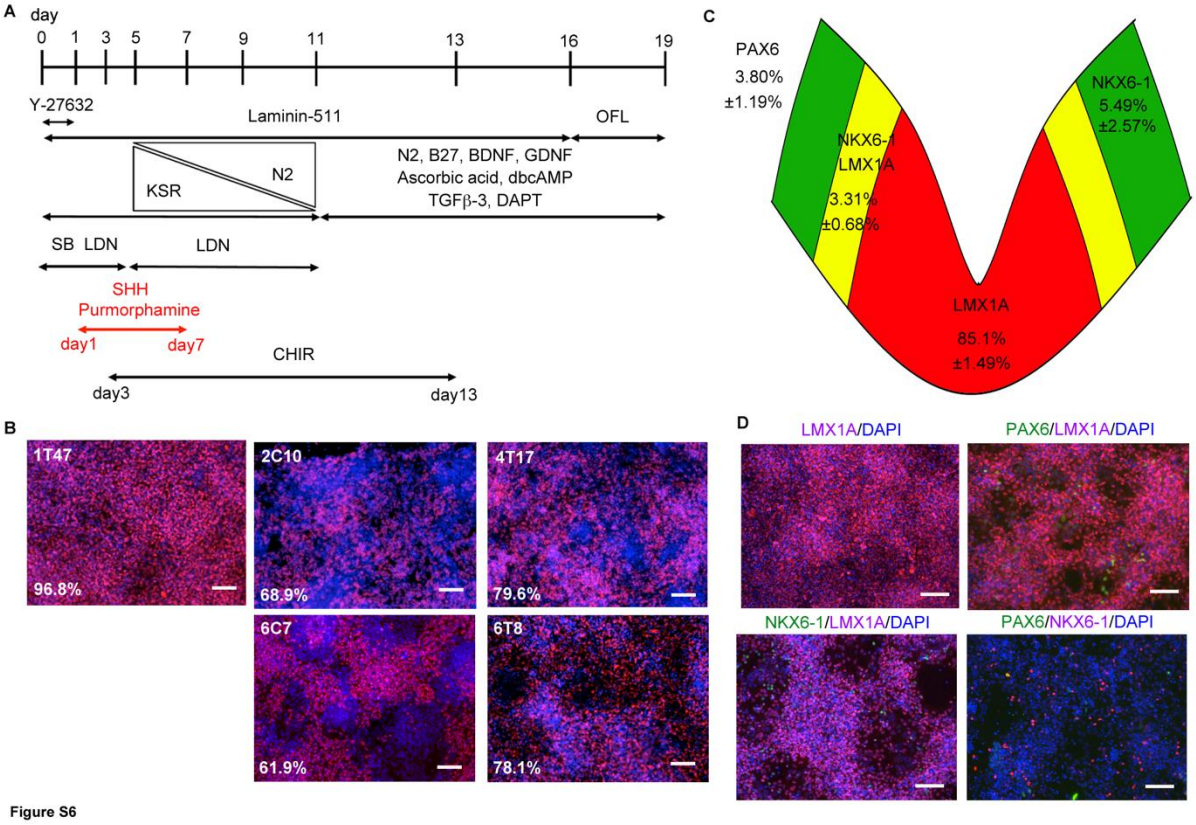

Figure S6 (related to Figure 5)

Figure S6. Differentiation capabilities of default-elite and non-elite clones. (A) Schematic representation of the differentiation protocol (proposed by Steinbeck et al. (2015) with slight modification). SB, SB431542; LDN, LDN193189; CHIR, CHIR99021; OFL, ornithine, fibronectin, and Laminin (iMatrix-511). (B) Immunostaining of induced cells on day 19. 1T47 is a default- and differentiation-elite clone, and the other clones are non-default-elite clones. The percentages shown indicate the ratios of FOXA2-positive cells (n = 1). (C) Schematic representation of the developing mouse midbrain region with its marker (adapted from Duan et al., 2013 and Andersson et al., 2006). Red shading, LMX1A-positive region; yellow shading, LMX1A and NKX6-1 double-positive regions; green, NKX6-1-positive region; white shading, more lateral region. The percentages show the ratios of each cell type in the induced 1T47 clone on day 19. The values represent the mean ± standard deviation (n = 3). (D) Immunostaining of midbrain-region markers in induced 1T47 cells. Blue, DAPI-positive;

green, NKX6-1- or PAX6-positive; red, LMX1A- or NKX6-1-positive (n = 3). Scale bars, 50 µm.

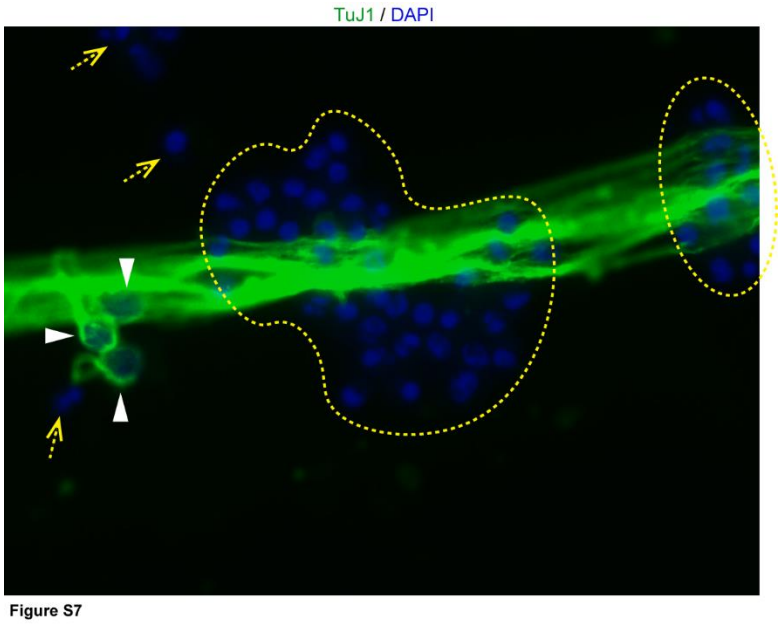

Figure S7 (related to Figure 5)

Figure S7. Preparatory histological examination to avoid counting dead cells. Pyknotic nuclei with a vigorous blue intensity (yellow arrows and dotted circles) were not counted as the cells did not express TuJ1, a pan-ectodermal marker, and were considered dead or dying. A few cells appeared to be stained with TuJ1 (white arrowheads). Based on the bundled appearance of the TuJ1-positive fibers, we believe that they represent both neuronal and radial glial projections.

Supplementary Table 1

Ratio of ventral midbrain markers in each mDA differentiation experiment.

The ratios of positive cells are shown in percentage for each midbrain dopaminergic differentiation experiment in triplicate.

(Related to Figure 5)

Clone	**LMX1A**	**NKX6-1**	**PAX6**	**NKX6-1/LMX1A**	**Total**
1T47	92.09	6.08	3.04	0.34	100.83
	93.49	5.00	2.48	1.49	99.46
	90.83	8.50	2.46	4.92	96.87
6T9	95.11	3.99	1.72	0.24	100.58
	86.74	6.54	0.66	2.79	91.15
	82.97	10.06	1.60	4.72	89.92
6T20	93.51	3.68	2.22	0.06	99.35
	83.85	6.58	0.47	3.17	87.73
	54.45	43.69	2.93	15.49	85.58
6C4	82.83	14.88	1.42	10.54	88.60
	75.31	19.26	1.37	5.42	90.52
	88.34	14.37	0.59	4.57	98.72
6C6	85.45	5.65	1.52	1.81	90.81
	74.41	6.22	1.43	1.20	80.86
	85.06	7.13	0.90	1.79	91.30

Supplementary Table 2

Sequences of the primers used in this study

(Related to STAR Methods)

gDNA detection primers	Sequences (5’-xxxx-3’)
CFTRexon24-F	GGCAGTACGATTCCATCCAG
CFTRexon24-R	GAAAGAGCTTCACCCTGTCG

Episomal vector detection primers	Sequences (5’-xxxx-3’)
pEP4-SF1	TTCCACGAGGGTAGTGAACC
pEP4-SR1	TCGGGGGTGTTAGAGACAAC
pEP4-SR3	CAGGCGAAGATTCAGGAGAG

For quantitative PCR analysis		
Target	Forward sequence (5’-xxxx-3’)	Reverse sequence (5’-xxxx-3’)
GAPDH	GCTCTCTGCTCCTCCTGTTC	GCCCAATACGACCAAATCC
NANOG	TCTCCAACATCCTGAACCTCA	TTGCTATTCTTCGGCCAGTT
POU5F1	CTTTGAGGCTCTGCAGCTTAG	TCTGCTTTGCATATCTCCTGAA
SOX2	GGGGGAATGGACCTTGTATAG	GCAAAGCTCCTACCGTACCA
KLF4	GCCGCTCCATTACCAAGA	TCTTCCCCTCTTTGGCTTG
MYC	TGCTCCATGAGGAGACACC	CTTTTCCACAGAAACAACATCG
MYCN	CCCTGAGCGATTCAGATGATGA	TTGGTGTTGGAGGAGGAACG
SOX21	GGGGCCCGGTTTGTATGTA	GAATTCACAGGCCTGCTCGC
SOX3	TCAAGAACCCCGTAGGGACA	CTGCGTTCGCACTACTCTTG
SOX1	GGCTGAGCACCACTACGACT	GCATTATAAAATTTCCCAAATCATC
PAX6	ACCCATTATCCAGATGTGTTTGCCCGAG	ATGGTGAAGCTGGGCATAGGCGGCAG
HES5	AGCACAGCAAAGCCTTCGTC	CTGCAGGCACCACGAGTAG
TBXT	GCTGTGACAGGTACCCAACC	CATGCAGGTGAGTTGTCAGAA

NLRP7	GCTGGAAGCAAGACCTGACC	CTAGCTGGGGCGATGTCATA
DPPA3	CAATTTGAGGCTCTGTCATCAG	ATCGGCGTCTTGACACAAC
DNMT3L	TCAAGGCTAACCAGCGAAAT	GCTGTGTGTGAACCTGGAGA
HHLA1	GAGTCCAACTGGTCTCCTGG	AGATCAGTAGCACCCCCTGA
ARRB1	CACGAAGACACGAACTTGGC	GGATGCAAGATCTCCCAACAG
FZD10	TGAGTTGGCTTTGCTACCCA	CCTGGGGATGGCTCATTTGT
GBX2	GGTAACTTCGACAAGGCGGAGG	GGTCGTCTTCCACCTTTGACTCG
NPTX1	CATCAATGACAAGGTGGCCAAG	TGATAGGGCGCCAAGTTCTC
POU3F1	GCTCGAGAGCCACTTTCTCA	CCAGGCGCGTATACATCGT
SIX3	CCGGAAGAGTTGTCCATGTTC	CGACTCGTGTTTGTTGATGGC
HAND1	ACCAGCTACATCGCCTACCT	CCTTTTCCGCTTGCTCTCAC
TET1	CCAAGCCCCAGAAGATTTAG	TGGAGCTAATCGTGTAGCCA
KLF4	TGCGGCAAAACCTACACAAAG	GTTCATCTGAGCGGGCGAAT
BMP4	TCCACAGCACTGGTCTTGAG	GGGATGTTCTCCAGATGTTCTT
GATA3	CTGTCCTTTGGACCACACCA	TCCATCGCGTTTAGGCTTCA
TWIST1	AGCTACGCCTTCTCGGTCTG	TGTCCATTTTCTCCTTCTCTGGA
ACTC1	AAGATGTGTGACGACGAGGAG	CTCTGGGCTTCATCACCTACG

REFERENCES

Andersson, E., Tryggvason, U., Deng, Q., Friling, S., Alekseenko, Z., Robert, B., Perlmann, T., and Ericson, J. (2006). Identification of intrinsic determinants of midbrain dopamine neurons. Cell 124, 393–405. 10.1016/j.cell.2005.10.037.

Arenas, E., Denham, M., and Villaescusa, J.C. (2015). How to make a midbrain dopaminergic neuron. Development 142, 1918–1936. 10.1242/dev.097394.

Barker, R.A., Parmar, M., Studer, L., and Takahashi, J. (2017). Human trials of stem cell-derived dopamine neurons for Parkinson's disease: dawn of a new era. Cell Stem Cell 21, 569–573. 10.1016/j.stem.2017.09.014.

Bartoccetti, M., van der Veer, B.K., Luo, X., Khoueiry, R., She, P., Bajaj, M., Xu, J., Janiszewski, A., Thienpont, B., Pasque, V., et al. (2020). Regulatory dynamics of Tet1 and Oct4 resolve stages of global DNA demethylation and transcriptomic changes in reprogramming. Cell Rep. 30, 2150–2169.e9. 10.1016/j.celrep.2020.01.065.

Bhaduri, A., Andrews, M.G., Mancia Leon, W., Jung, D., Shin, D., Allen, D., Jung, D., Schmunk, G., Haeussler, M., Salma, J., et al. (2020). Cell stress in cortical organoids impairs molecular subtype specification. Nature 578, 142–148. 10.1038/s41586-020-1962-0.

Blauwkamp, T.A., Nigam, S., Ardehali, R., Weissman, I.L., and Nusse, R. (2012). Endogenous Wnt signalling in human embryonic stem cells generates an equilibrium of distinct lineage-specified progenitors. Nat. Commun. 3, 1070. 10.1038/ncomms2064.

Boles, N.C., Hirsch, S.E., Le, S., Corneo, B., Najm, F., Minotti, A.P., Wang, Q., Lotz, S., Tesar, P.J., and Fasano, C.A. (2014). NPTX1 regulates neural lineage specification from human pluripotent stem cells. Cell Rep. 6, 724–736. 10.1016/j.celrep.2014.01.026.

Bose, A., Petsko, G.A., and Studer, L. (2022). Induced pluripotent stem cells: a tool for modeling Parkinson's disease. Trends Neurosci. 45, 608–620. 10.1016/j.tins.2022.05.001.

Bouhon, I.A., Kato, H., Chandran, S., and Allen, N.D. (2005). Neural differentiation of mouse embryonic stem cells in chemically defined medium. Brain Res. Bull. 68, 62–75. 10.1016/j.brainresbull.2005.08.022.

Butler, A., Hoffman, P., Smibert, P., Papalexi, E., and Satija, R. (2018). Integrating single-cell transcriptomic data across different conditions, technologies, and species. Nat. Biotechnol. 36, 411–420. 10.1038/nbt.4096.

Cacchiarelli, D., Trapnell, C., Ziller, M.J., Soumillon, M., Cesana, M., Karnik, R., Donaghey, J., Smith, Z.D., Ratanasirintrawoot, S., Zhang, X., et al. (2015). Integrative analyses of human reprogramming reveal dynamic nature of induced pluripotency. Cell 162, 412–424. 10.1016/j.cell.2015.06.016.

Chambers, S.M., Fasano, C.A., Papapetrou, E.P., Tomishima, M., Sadelain, M., and Studer, L. (2009). Highly efficient neural conversion of human ES and iPS cells by dual inhibition of SMAD signaling. Nat. Biotechnol. 27, 275–280. 10.1038/nbt.1529.

Charlton, J., Jung, E.J., Mattei, A.L., Bailly, N., Liao, J., Martin, E.J., Giesselmann, P., Brändl, B., Stamenova, E.K., Müller, F.J., et al. (2020). TETs compete with DNMT3 activity in pluripotent cells at thousands of methylated somatic enhancers. Nat. Genet. 52, 819–827. 10.1038/s41588-020-0639-9.

Chen, G., Gulbranson, D.R., Hou, Z., Bolin, J.M., Ruotti, V., Probasco, M.D., Smuga-Otto, K., Howden, S.E., Diol, N.R., Propson, N.E., et al. (2011). Chemically defined conditions for human iPSC derivation and culture. Nat. Methods 8, 424–429. 10.1038/nmeth.1593.

Chhabra, S., and Warmflash, A. (2021). BMP-treated human embryonic stem cells transcriptionally resemble amnion cells in the monkey embryo. Biol. Open 10. 10.1242/bio.058617.

Chin, M.H., Mason, M.J., Xie, W., Volinia, S., Singer, M., Peterson, C., Ambartsumyan, G., Aimiuwu, O., Richter, L., Zhang, J., et al. (2009). Induced pluripotent stem cells and

embryonic stem cells are distinguished by gene expression signatures. Cell Stem Cell 5, 111–123. 10.1016/j.stem.2009.06.008.

Dobin, A., Davis, C.A., Schlesinger, F., Drenkow, J., Zaleski, C., Jha, S., Batut, P., Chaisson, M., and Gingeras, T.R. (2013). STAR: ultrafast universal RNA-seq aligner. Bioinformatics 29, 15–21. 10.1093/bioinformatics/bts635.

Duan, D., Fu, Y., Paxinos, G., and Watson, C. (2013). Spatiotemporal expression patterns of Pax6 in the brain of embryonic, newborn, and adult mice. Brain Struct. Funct. 218, 353–372. 10.1007/s00429-012-0397-2.

Ferri, A.L., Lin, W., Mavromatakis, Y.E., Wang, J.C., Sasaki, H., Whitsett, J.A., and Ang, S.L. (2007). Foxa1 and Foxa2 regulate multiple phases of midbrain dopaminergic neuron development in a dosage-dependent manner. Development 134, 2761–2769. 10.1242/dev.000141.

Fogarty, N.M.E., McCarthy, A., Snijders, K.E., Powell, B.E., Kubikova, N., Blakeley, P., Lea, R., Elder, K., Wamaitha, S.E., Kim, D., et al. (2017). Genome editing reveals a role for OCT4 in human embryogenesis. Nature 550, 67–73. 10.1038/nature24033.

Hu, X., Zhang, L., Mao, S.Q., Li, Z., Chen, J., Zhang, R.R., Wu, H.P., Gao, J., Guo, F., Liu, W., et al. (2014). Tet and TDG mediate DNA demethylation essential for mesenchymal-to-epithelial transition in somatic cell reprogramming. Cell Stem Cell 14, 512–522. 10.1016/j.stem.2014.01.001.

International Stem Cell Initiative. (2007). Characterization of human embryonic stem cell lines by the International Stem Cell Initiative. Nat. Biotechnol. 25, 803–816. 10.1038/nbt1318.

Kim, H., Lee, G., Ganat, Y., Papapetrou, E.P., Lipchina, I., Socci, N.D., Sadelain, M., and Studer, L. (2011). miR-371-3 expression predicts neural differentiation propensity in human pluripotent stem cells. Cell Stem Cell 8, 695–706. 10.1016/j.stem.2011.04.002.

Kim, J., Koo, B.K., and Knoblich, J.A. (2020). Human organoids: model systems for human biology and medicine. Nat. Rev. Mol. Cell Biol. 21, 571–584. 10.1038/s41580-020-0259-3.

Kim, T.W., Piao, J., Koo, S.Y., Kriks, S., Chung, S.Y., Betel, D., Socci, N.D., Choi, S.J., Zabierowski, S., Dubose, B.N., et al. (2021). Biphasic activation of WNT signaling facilitates the derivation of midbrain dopamine neurons from hESCs for translational use. Cell Stem Cell 28, 343–355.e5. 10.1016/j.stem.2021.01.005.

Koyanagi-Aoi, M., Ohnuki, M., Takahashi, K., Okita, K., Noma, H., Sawamura, Y., Teramoto, I., Narita, M., Sato, Y., Ichisaka, T., et al. (2013). Differentiation-defective phenotypes revealed by large-scale analyses of human pluripotent stem cells. Proc. Natl. Acad. Sci. U. S. A. 110, 20569–20574. 10.1073/pnas.1319061110.

La Manno, G., Gyllborg, D., Codeluppi, S., Nishimura, K., Salto, C., Zeisel, A., Borm, L.E., Stott, S.R.W., Toledo, E.M., Villaescusa, J.C., et al. (2016). Molecular diversity of midbrain development in mouse, human, and stem cells. Cell 167, 566–580.e19. 10.1016/j.cell.2016.09.027.

Li, B., and Dewey, C.N. (2011). RSEM: accurate transcript quantification from RNA-Seq data with or without a reference genome. BMC Bioinformatics 12, 323. 10.1186/1471-2105-12-323.

Li, R., Liang, J., Ni, S., Zhou, T., Qing, X., Li, H., He, W., Chen, J., Li, F., Zhuang, Q., et al. (2010). A mesenchymal-to-epithelial transition initiates and is required for the nuclear reprogramming of mouse fibroblasts. Cell Stem Cell 7, 51–63. 10.1016/j.stem.2010.04.014.

Liang, G., and Zhang, Y. (2013). Genetic and epigenetic variations in iPSCs: potential causes and implications for application. Cell Stem Cell 13, 149–159. 10.1016/j.stem.2013.07.001.

Lister, R., Pelizzola, M., Kida, Y.S., Hawkins, R.D., Nery, J.R., Hon, G., Antosiewicz-Bourget, J., O'Malley, R., Castanon, R., Klugman, S., et al. (2011). Hotspots of aberrant

epigenomic reprogramming in human induced pluripotent stem cells. Nature 471, 68–73. 10.1038/nature09798.

Loh, K.M., Chen, A., Koh, P.W., Deng, T.Z., Sinha, R., Tsai, J.M., Barkal, A.A., Shen, K.Y., Jain, R., Morganti, R.M., et al. (2016). Mapping the pairwise choices leading from pluripotency to human bone, heart, and other mesoderm cell types. Cell 166, 451–467. 10.1016/j.cell.2016.06.011.

Loh, K.M., and Lim, B. (2011). A precarious balance: pluripotency factors as lineage specifiers. Cell Stem Cell 8, 363–369. 10.1016/j.stem.2011.03.013.

Metzis, V., Steinhauser, S., Pakanavicius, E., Gouti, M., Stamataki, D., Ivanovitch, K., Watson, T., Rayon, T., Mousavy Gharavy, S.N., Lovell-Badge, R., et al. (2018). Nervous system regionalization entails axial allocation before neural differentiation. Cell 175, 1105–1118.e17. 10.1016/j.cell.2018.09.040.

Ohnishi, K., Semi, K., Yamamoto, T., Shimizu, M., Tanaka, A., Mitsunaga, K., Okita, K., Osafune, K., Arioka, Y., Maeda, T., et al. (2014). Premature termination of reprogramming in vivo leads to cancer development through altered epigenetic regulation. Cell 156, 663–677. 10.1016/j.cell.2014.01.005.

Ohnuki, M., Tanabe, K., Sutou, K., Teramoto, I., Sawamura, Y., Narita, M., Nakamura, M., Tokunaga, Y., Nakamura, M., Watanabe, A., et al. (2014). Dynamic regulation of human endogenous retroviruses mediates factor-induced reprogramming and differentiation potential. Proc. Natl. Acad. Sci. U. S. A. 111, 12426–12431. 10.1073/pnas.1413299111.

Okita, K., Matsumura, Y., Sato, Y., Okada, A., Morizane, A., Okamoto, S., Hong, H., Nakagawa, M., Tanabe, K., Tezuka, K., et al. (2011). A more efficient method to generate integration-free human iPS cells. Nat. Methods 8, 409–412. 10.1038/nmeth.1591.

Ono, T., Suzuki, Y., Kato, Y., Fujita, R., Araki, T., Yamashita, T., Kato, H., Torii, R., and Sato, N. (2014). A single-cell and feeder-free culture system for monkey embryonic stem cells. PLOS ONE 9, e88346. 10.1371/journal.pone.0088346.

Osafune, K., Caron, L., Borowiak, M., Martinez, R.J., Fitz-Gerald, C.S., Sato, Y., Cowan, C.A., Chien, K.R., and Melton, D.A. (2008). Marked differences in differentiation propensity among human embryonic stem cell lines. Nat. Biotechnol. 26, 313–315. 10.1038/nbt1383.

Ozair, M.Z., Kintner, C., and Brivanlou, A.H. (2013). Neural induction and early patterning in vertebrates. Wiley Interdiscip. Rev. Dev. Biol. 2, 479–498. 10.1002/wdev.90.

Patani, R., Compston, A., Puddifoot, C.A., Wyllie, D.J., Hardingham, G.E., Allen, N.D., and Chandran, S. (2009). Activin/Nodal inhibition alone accelerates highly efficient neural conversion from human embryonic stem cells and imposes a caudal positional identity. PLOS ONE 4, e7327. 10.1371/journal.pone.0007327.

Ruetz, T., Pfisterer, U., Di Stefano, B., Ashmore, J., Beniazza, M., Tian, T.V., Kaemena, D.F., Tosti, L., Tan, W., Manning, J.R., et al. (2017). Constitutively active SMAD2/3 are broad-scope potentiators of transcription-factor-mediated cellular reprogramming. Cell Stem Cell 21, 791–805.e9. 10.1016/j.stem.2017.10.013.

Samavarchi-Tehrani, P., Golipour, A., David, L., Sung, H.K., Beyer, T.A., Datti, A., Woltjen, K., Nagy, A., and Wrana, J.L. (2010). Functional genomics reveals a BMP-driven mesenchymal-to-epithelial transition in the initiation of somatic cell reprogramming. Cell Stem Cell 7, 64–77. 10.1016/j.stem.2010.04.015.

Sasaki, K., Nakamura, T., Okamoto, I., Yabuta, Y., Iwatani, C., Tsuchiya, H., Seita, Y., Nakamura, S., Shiraki, N., Takakuwa, T., et al. (2016). The germ cell fate of cynomolgus monkeys is specified in the nascent amnion. Dev. Cell 39, 169–185. 10.1016/j.devcel.2016.09.007.

Shao, Y., Taniguchi, K., Gurdziel, K., Townshend, R.F., Xue, X., Yong, K.M.A., Sang, J., Spence, J.R., Gumucio, D.L., and Fu, J. (2017). Self-organized amniogenesis by human pluripotent stem cells in a biomimetic implantation-like niche. Nat. Mater. 16, 419–425. 10.1038/nmat4829.

Simunovic, M., and Brivanlou, A.H. (2017). Embryoids, organoids and gastruloids: new approaches to understanding embryogenesis. Development 144, 976–985. 10.1242/dev.143529.

Steinbeck, J.A., Choi, S.J., Mrejeru, A., Ganat, Y., Deisseroth, K., Sulzer, D., Mosharov, E.V., and Studer, L. (2015). Optogenetics enables functional analysis of human embryonic stem cell-derived grafts in a Parkinson's disease model. Nat. Biotechnol. 33, 204–209. 10.1038/nbt.3124.

Tao, Y., and Zhang, S.C. (2016). Neural subtype specification from human pluripotent stem cells. Cell Stem Cell 19, 573–586. 10.1016/j.stem.2016.10.015.

Tchieu, J., Zimmer, B., Fattahi, F., Amin, S., Zeltner, N., Chen, S., and Studer, L. (2017). A modular platform for differentiation of human PSCs into all major ectodermal lineages. Cell Stem Cell 21, 399–410.e7. 10.1016/j.stem.2017.08.015.

Tyser, R.C.V., Mahammadov, E., Nakanoh, S., Vallier, L., Scialdone, A., and Srinivas, S. (2021). Single-cell transcriptomic characterization of a gastrulating human embryo. Nature 600, 285–289. 10.1038/s41586-021-04158-y.

Verma, N., Pan, H., Doré, L.C., Shukla, A., Li, Q.V., Pelham-Webb, B., Teijeiro, V., González, F., Krivtsov, A., Chang, C.J., et al. (2018). TET proteins safeguard bivalent promoters from de novo methylation in human embryonic stem cells. Nat. Genet. 50, 83–95. 10.1038/s41588-017-0002-y.

Xiang, L., Yin, Y., Zheng, Y., Ma, Y., Li, Y., Zhao, Z., Guo, J., Ai, Z., Niu, Y., Duan, K., et al. (2020). A developmental landscape of 3D-cultured human pre-gastrulation embryos. Nature 577, 537–542. 10.1038/s41586-019-1875-y.

Yin, X., Mead, B.E., Safaee, H., Langer, R., Karp, J.M., and Levy, O. (2016). Engineering stem cell organoids. Cell Stem Cell 18, 25–38. 10.1016/j.stem.2015.12.005.

Yu, J., Hu, K., Smuga-Otto, K., Tian, S., Stewart, R., Slukvin, I.I., and Thomson, J.A. (2009). Human induced pluripotent stem cells free of vector and transgene sequences. Science 324, 797–801. 10.1126/science.1172482.

Zhang, X., Huang, C.T., Chen, J., Pankratz, M.T., Xi, J., Li, J., Yang, Y., Lavaute, T.M., Li, X.J., Ayala, M., et al. (2010). Pax6 is a human neuroectoderm cell fate determinant. Cell Stem Cell 7, 90–100. 10.1016/j.stem.2010.04.017.

Zheng, Y., Xue, X., Shao, Y., Wang, S., Esfahani, S.N., Li, Z., Muncie, J.M., Lakins, J.N., Weaver, V.M., Gumucio, D.L., et al. (2019). Controlled modelling of human epiblast and amnion development using stem cells. Nature 573, 421–425. 10.1038/s41586-019-1535-2.